

Autonomous aerial cinematography in unstructured environments with learned artistic decision-making

Rogerio Bonatti¹  | Wenshan Wang¹  | Cherie Ho¹  | Aayush Ahuja¹ |
Mirko Gschwindt²  | Efe Camci³  | Erdal Kayacan⁴  | Sanjiban Choudhury⁵  |
Sebastian Scherer¹ 

¹The Robotics Institute, Carnegie Mellon University, Pittsburgh, Pennsylvania

²Department of Computer Science, Technische Universität München, Munich, Germany

³School of Mechanical and Aerospace Engineering, Nanyang Technological University, Singapore, Singapore

⁴Department of Engineering, Aarhus University, Aarhus, Denmark

⁵School of Computer Science, University of Washington, Seattle, Washington

Correspondence

Rogerio Bonatti, Robotics Institute, Carnegie Mellon University, Pittsburgh, PA 15213.
Email: rbonatti@cs.cmu.edu

Funding information

Yamaha Motor Co., Ltd.,
Grant/Award Number: A019969

Abstract

Aerial cinematography is revolutionizing industries that require live and dynamic camera viewpoints such as entertainment, sports, and security. However, safely piloting a drone while filming a moving target in the presence of obstacles is immensely taxing, often requiring multiple expert human operators. Hence, there is a demand for an autonomous cinematographer that can reason about both geometry and scene context in real-time. Existing approaches do not address all aspects of this problem; they either require high-precision motion-capture systems or global positioning system tags to localize targets, rely on prior maps of the environment, plan for short time horizons, or only follow fixed artistic guidelines specified before the flight. In this study, we address the problem in its entirety and propose a complete system for real-time aerial cinematography that for the first time combines: (a) vision-based target estimation; (b) 3D signed-distance mapping for occlusion estimation; (c) efficient trajectory optimization for long time-horizon camera motion; and (d) learning-based artistic shot selection. We extensively evaluate our system both in simulation and in field experiments by filming dynamic targets moving through unstructured environments. Our results indicate that our system can operate reliably in the real world without restrictive assumptions. We also provide in-depth analysis and discussions for each module, with the hope that our design tradeoffs can generalize to other related applications. Videos of the complete system can be found at <https://youtu.be/ookhHnqmlaU>.

KEY WORDS

aerial robotics, cinematography, computer vision, learning, mapping, motion planning

1 | INTRODUCTION

Manually operated unmanned aerial vehicles (UAVs) are drastically improving efficiency and productivity in a diverse set of industries and economic activities. In particular, tasks that require dynamic camera viewpoints have been most affected, where the development of small scale UAVs has alleviated the need for sophisticated hardware to manipulate cameras in space. For instance, in the movie industry, drones are changing the way both professional and amateur

film-makers can capture shots of actors and landscapes by allowing the composition of aerial viewpoints that are not feasible using traditional devices such as hand-held cameras and dollies (Santamarina-Campos & Segarra-Oña, 2018). In the sports domain, flying cameras can track fast-moving athletes and accompany dynamic movements (La Bella, 2016). Furthermore, flying cameras show a largely unexplored potential for tracking subjects of interest in security applications (De-Miguel-Molina, 2018), which are not possible with static sensors.

However, manually operated UAVs often require multiple expert pilots due to the difficulty of executing all necessary perception and motion planning tasks synchronously: it takes high attention and effort to simultaneously identify the actor(s), predict how the scene is going to evolve, control the UAV, avoid obstacles, and reach the desired viewpoints. Hence, there is a need for an autonomous aerial cinematography system.

The distinctive challenge of developing an autonomous aerial cinematography system is the need to tightly couple *contextual* and *geometric* threads. Contextual reasoning involves processing camera images to detect the actor, understanding how the scene is going to evolve, and selecting desirable viewpoints. Geometric reasoning considers the 3D configuration of objects in the environment to evaluate the visibility quality of a particular viewpoint and whether the UAV can reach it in a safe manner. Although these two threads differ significantly in terms of sensing modalities, computational representation, and computational complexity, both sides play a vital role when addressing the entirety of the autonomous filming problem. In this study, we present a complete system that combines both threads in a cohesive and principled manner. To develop our autonomous cinematographer, we address several key challenges.

1.1 | Challenges

Consider a typical filming scenario in Figure 1. The UAV must overcome several challenges.

1.1.1 | Actor pose estimation with challenging visual inputs

The UAV films a dynamic actor from various angles, therefore, it is critical to accurately localize the actor's position and orientation

in a 3D environment. In practice, the use of external sensors such as motion capture systems (Nägeli, Meier, Domahidi, Alonso-Mora, & Hilliges, 2017) and global positioning system (GPS) tags (Bonatti, Zhang, Choudhury, Wang, & Scherer, 2018; Joubert et al., 2016) for pose estimation is highly impractical; a robust system should only rely on visual localization. The challenge is to deal with all possible viewpoints, scales, backgrounds, lighting conditions, motion blur caused by both the dynamic actor and camera.

1.1.2 | Operating in unstructured scenarios

The UAV flies in diverse, unstructured environments without prior information. In a typical mission, it follows an actor across varying terrain and obstacle types, such as slopes, mountains, and narrow trails between trees or buildings. The challenge is to maintain an online map that has a high enough resolution to reason about viewpoint occlusions and that updates itself fast enough to keep the vehicle safe.

1.1.3 | Keeping actor visibility while staying safe

In cinematography, the UAV must maintain visibility of the actor for as long as possible while staying safe in a partially known environment. When dealing with dynamic targets, the UAV must anticipate the actor's motion and reason about collisions and occlusions generated by obstacles in potential trajectories. The challenge of visibility has been explored in previous works in varying degrees of obstacle complexity (Bonatti, Ho, Wang, Choudhury, & Scherer, 2019; Galvane et al., 2018; Nägeli et al., 2017; Penin, Giordano, & Chaumette, 2018).

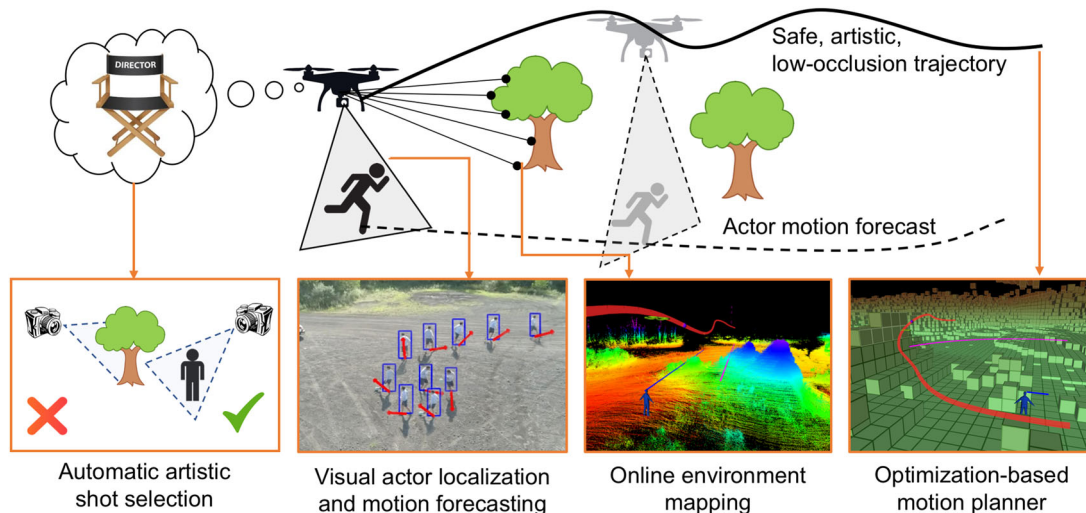


FIGURE 1 Aerial cinematographer pipeline: the unmanned aerial vehicle visually detects the actor's motion using a vision-based localization module, maps the environment with an onboard LiDAR sensor, reasons about artistic guidelines, and plans a smooth, collision-free trajectory while avoiding occlusions [Color figure can be viewed at wileyonlinelibrary.com]

1.1.4 | Understanding scene context for autonomous artistic decision-making

When filming a movie, the director actively selects the camera pose based on the actor's movement, environment characteristics, and intrinsic artistic values. Although humans can make such esthetic decisions implicitly, it is challenging to define explicit rules to define the ideal artistic choices for a given context.

1.1.5 | Making real-time decisions with onboard resources

Our focus is on unscripted scenarios where shots are decided on the fly; all algorithms must run in real-time with limited computational resources.

1.2 | Contributions

Our paper revolves around two key ideas. First, we design differentiable objectives for camera motion that can be efficiently optimized for long time horizons. We architect our system to compute these objectives efficiently online to film a dynamic actor. Second, we apply learning to elicit human artistic preferences in selecting a sequence of shots. Specifically, we offer the following contributions:

We propose a method for visually localizing the actor's position, orientation, and forecasting their future trajectory in the world coordinate frame. We present a novel semisupervised approach that uses temporal continuity in sequential data for the heading direction estimation problem (Section 5);

We propose an incremental signed distance transform algorithm for large-scale real-time environment mapping using a range sensor, for example, LiDAR (Section 6);

We formalize the aerial filming motion planning problem following cinematography guidelines for arbitrary types of shots and arbitrary obstacle shapes. We propose an efficient optimization-based motion planning method that exploits covariant gradients and Hessians of the objective functions for fast convergence (Section 7);

We propose a deep reinforcement learning (RL) method that incorporates human esthetic preferences for artistic reasoning to act as an autonomous movie director, considering the current scene context to select the next camera viewpoints (Section 8);

We offer extensive quantitative and qualitative performance evaluations both for our integrated system and for each module, both in simulation and field tests (Section 9), along with detailed discussions on experimental lessons learned (Section 10).

This paper builds upon our previous works that each focuses on an individual component of our framework: visual actor detection, tracking, and heading estimation (W. Wang, Ahuja, Zhang, Bonatti, & Scherer, 2019), online environment mapping (Bonatti et al., 2019),

motion planning for cinematography (Bonatti et al., 2018), and autonomous artistic viewpoint selection (Gschwindt, Camci, Bonatti, Wang, & Scherer, 2019). In this paper, for the first time, we present a detailed description of the unified architecture (Section 4), provide implementation details of the entire framework, and offer extensive flight test evaluations of the complete system.

2 | PROBLEM DEFINITION

The overall task is to control a UAV to film an actor who is moving through an unknown environment. Let $\xi_q(t) : [0, t_f] \rightarrow \mathbb{R}^3 \times SO(2)$ be the trajectory of the UAV as a mapping from time to a position and heading, that is, $\xi_q(t) = \{x_q(t), y_q(t), z_q(t), \psi_q(t)\}$. Analogously, let $\xi_a(t) : [0, t_f] \rightarrow \mathbb{R}^3 \times SO(2)$ be the trajectory of the actor: $\xi_a(t) = \{x_a(t), y_a(t), z_a(t), \psi_a(t)\}$. In our work, an instantaneous measurement of the actor state $S_a : \mathbb{R}^3 \times SO(2)$ is obtained using onboard sensors (monocular camera and LiDAR, as seen in Section 5), but external sensors and motion capture systems could also be employed (Section 3). Measurements S_a are continuously fed into a prediction module that computes ξ_a (Section 5).

The UAV also needs to store a representation of the environment. Let grid $\mathcal{G} : \mathbb{R}^3 \rightarrow [0, 1]$ be a voxel occupancy grid that maps every point in space to a probability of occupancy. Let $\mathcal{M} : \mathbb{R}^3 \rightarrow \mathbb{R}$ be the signed distance value of a point to the nearest obstacle. Positive signs are for points in free space, and negative signs are for points either in occupied or unknown space, which we assume to be potentially inside an obstacle. During the flight the UAV senses the environment with the onboard LiDAR, updates grid \mathcal{G} , and then updates \mathcal{M} (more details at Section 6).

We can generically formulate a motion planning problem that aims to minimize a particular cost function $J(\xi_q)$ for cinematography. Within the filming context, this cost function measures jerkiness of motion, safety, environmental occlusion of the actor, and shot quality (artistic quality of viewpoints). This cost function depends on the environment \mathcal{G} and \mathcal{M} , and on the actor forecast ξ_a , all of which are sensed on-the-fly. The changing nature of the environment and ξ_a demands replanning at a high frequency.

Here we briefly touch upon the four components of the cost function $J(\xi_q)$ (refer to Section 7 for details and mathematical expressions):

Smoothness $J_{\text{smooth}}(\xi_q)$: Penalizes jerky motions that may lead to camera blur and unstable flight;

Safety $J_{\text{obs}}(\xi_q, \mathcal{M})$: Penalizes proximity to obstacles that are unsafe for the UAV;

Occlusion $J_{\text{occ}}(\xi_q, \xi_a, \mathcal{M})$: Penalizes occlusion of the actor by obstacles in the environment;

Shot quality $J_{\text{shot}}(\xi_q, \xi_a, \Omega_{\text{art}})$: Penalizes poor viewpoint angles and scales that deviate from the desired artistic guidelines, given by the set of parameters Ω_{art} .

In its simplest form, we can express $J(\xi_q)$ as a linear composition of each individual cost, weighted by scalars λ_i . The objective is to

minimize $J(\xi_q)$ subject to initial-boundary constraints $\xi_q(0)$. The solution ξ_q^* is then tracked by the UAV:

$$J(\xi_q) = [1 \ \lambda_1 \ \lambda_2 \ \lambda_3] \begin{bmatrix} J_{\text{smooth}}(\xi_q) \\ J_{\text{obs}}(\xi_q, M) \\ J_{\text{occ}}(\xi_q, \xi_a, M) \\ J_{\text{shot}}(\xi_q, \xi_a, \Omega_{\text{art}}) \end{bmatrix}, \quad (1)$$

$$\xi_q^* = \arg \min_{\xi_q} J(\xi_q), \quad \text{s.t. } \xi_q(0) = \{x_0, y_0, z_0, \psi_0\}.$$

We describe in Section 7 how (1) is solved. The parameters Ω_{art} of the shot quality term J_{shot} are usually specified by the user before takeoff, and assumed constant throughout the flight. For instance, based on the terrain characteristics and the type of motion the user expects the actor to do, they may specify a frontal or circular shot with a particular scale to be the best artistic choice for that context. Alternatively, Ω_{art} can change dynamically, either by a user's choice or algorithmically.

A dynamically changing Ω_{art} leads to a new challenge: the UAV must make choices that maximize the artistic value of the incoming visual feed. As explained further in Section 8, artistic choices affect not only the immediate images recorded by the UAV. By changing the positioning of the UAV relative to the subject and obstacles, current choices influence the images captured in future time steps. Therefore, the selection of Ω_{art} needs to be framed as a sequential decision-making process.

Let $v_t = \{I_1, I_2, \dots, I_k\}$ be a sequence of k observed images captured by the UAV during time step t between consecutive artistic decisions. Let $R_{\text{art}}(v_t)$ be the user's implicit evaluation reward based on the observed video segment v_t . The user's choice of an optimal artistic parameter sequence $\{\Omega_1^*, \Omega_2^*, \dots, \Omega_n^*\}$ can be interpreted as an optimization of the following form:

$$\{\Omega_1^*, \Omega_2^*, \dots, \Omega_n^*\} = \arg \max_{\{\Omega_1, \Omega_2, \dots, \Omega_n\}} \sum_t R_{\text{art}}(v_t). \quad (2)$$

The optimization from Equation (2) is usually left up to the UAV operator's experience and intuition. In Section 8, we detail a novel method for implicitly learning the selection of artistic parameters depending on the scene's context.

3 | RELATED WORK

Our work exploits synergies at the confluence of several domains of research to develop an aerial cinematography platform that can follow dynamic targets in unstructured environments using onboard sensors and computing power. Next, we describe related works in different areas that come together under the problem definition described in Section 2.

3.1 | Virtual cinematography

Camera control in virtual cinematography has been extensively examined by the computer graphics community as reviewed by

Christie, Olivier, and Normand (2008). These methods typically reason about the utility of a viewpoint in isolation, follow artistic principles and composition rules (Arijon, 1976; Bowen & Thompson, 2013) and employ either optimization-based approaches to find good viewpoints or reactive approaches to track the virtual actor. The focus is typically on through-the-lens control where a virtual camera is manipulated while maintaining focus on certain image features (Drucker & Zeltzer, 1994; Gleicher & Witkin, 1992; Lino & Christie, 2015; Lino, Christie, Ranon, & Bares, 2011). However, virtual cinematography is free of several real-world limitations such as robot physics constraints and assumes full knowledge of the environment.

Several works analyse the choice of which viewpoint to employ for a particular situation. For example, in Drucker and Zeltzer (1994), the researchers use an A* planner to move a virtual camera in precomputed indoor simulation scenarios to avoid collisions with obstacles in 2D. More recently, we find works such as Leake, Davis, Truong, and Agrawala (2017) that postprocesses videos of a scene taken from different angles by automatically labeling features of different views. The approach uses high-level user-specified rules which exploit the labels to automatically select the optimal sequence of viewpoints for the final movie. In addition, Wu, Palù, Ranon, and Christie (2018) help editors by defining a formal language of editing patterns for movies.

3.2 | Autonomous aerial cinematography

There is a rich history of work in autonomous aerial filming. For instance, several works focus on following user-specified artistic guidelines (Galvane, Fleureau, Tariolle, & Guillotel, 2017, 2018; Joubert et al., 2016; Nägeli et al., 2017) but often rely on perfect actor localization through a high-precision RTK GPS or a motion-capture system. Additionally, although the majority of work in the area deals with collisions between UAVs and actors (Huang, Gao, et al., 2018; Joubert et al., 2016; Nägeli et al., 2017), they do not factor in the environment for safety considerations. While there are several successful commercial products, they too have certain limitations such as operating in low speed and low clutter regimes (e.g., DJI Mavic; DJI, 2018) or relatively short planning horizons (e.g., Skydio R1; Skydio, 2018). Even our previous work (Bonatti et al., 2018), despite handling environmental occlusions and collisions, assumes a prior elevation map and uses GPS to localize the actor. Such simplifications impose restrictions on the diversity of scenarios that the system can handle.

Several contributions to aerial cinematography focus on key-frame navigation. Gebhardt, Hepp, Nägeli, Stevšić, and Hilliges (2016, 2018), Joubert, Roberts, Truong, Berthouzoz, and Hanrahan (2015), Roberts and Hanrahan (2016), and Xie et al. (2018) provide user interface tools to retime and connect static aerial viewpoints to provide smooth and dynamically feasible trajectories, as well as a visually pleasing images. Lan, Shridhar, Hsu, and Zhao, (2017) use key-frames defined on the image itself instead of world coordinates.

Other works focus on tracking dynamic targets and employ a diverse set of techniques for actor localization and navigation. For example, Huang, Gao, et al. (2018) and Huang, Yang, et al. (2018) detect the skeleton of targets from visual input, while other approaches rely on off-board actor localization methods from either motion-capture systems or GPS sensors (Bonatti et al., 2018; Galvane et al., 2017, 2018; Joubert et al., 2016; Nägeli et al., 2017). These approaches have varying levels of complexity: Bonatti et al. (2018) and Galvane et al. (2018) can avoid obstacles and occlusions with the environment and with actors, while other approaches only handle collisions and occlusions caused by actors. In addition, in our latest work Bonatti et al. (2019) we made two important improvements on top of Bonatti et al. (2018) by including visual actor localization and online environment mapping.

Specifically, on the motion planning side, we note that different UAV applications can influence the choice of motion planning algorithms. The main motivation is that different types of planners can exploit specific properties and guarantees of the cost functions. For example, sampling-based planners (Elbanhawi & Simic, 2014; Karaman & Frazzoli, 2011; Kuffner & LaValle, 2000) or search-based planners (Aine, Swaminathan, Narayanan, Hwang, & Likhachev, 2016; LaValle, 2006) should ideally use fast-to-compute costs so that many different states can be explored during search in high-dimensional state spaces. Other categories of planners, based on trajectory optimization (Ratliff, Zucker, Bagnell, & Srinivasa, 2009; Schulman et al., 2013), usually require cost functions to be differentiable to the first or higher orders. We also find hybrid methods that make judicious use of optimization combined with search or sampling (Choudhury, Gammell, Barfoot, Srinivasa, & Scherer, 2016; Luna, Şucan, Moll, & Kavraki, 2013).

Furthermore, different systems present significant differences in onboard versus off-board computation. We summarize and compare contributions from past works in Table 1. It is important to notice that none of the previously published approaches provides a complete solution to the generic aerial cinematography problem using only onboard resources.

TABLE 1 Comparison of dynamic aerial cinematography systems

References	Online art. selec.	Online map	Actor localiz.	Onboard comp.	Avoids occl.	Avoids obst.	Online plan
Galvane et al. (2017)	✗	✗	✗	✗	✗	✗	✓
Joubert et al. (2016)	✗	✗	✗	✗	✗	Actor	✓
Nägeli et al. (2017)	✗	✗	✗	✗	Actor	Actor	✓
Galvane et al. (2018)	✗	✗	✗	✗	✓	✓	✓
Huang et al. (2018b)	✗	✗	✓	✓	✗	Actor	✓
Huang et al. (2018a)	Actor proj.	✗	✓	✓	✗	Actor	✓
Bonatti et al. (2018)	✗	✗	Vision	✓	✓	✓	✓
Bonatti et al. (2019)	✗	✓	✓	✓	✓	✓	✓
Ours	✓	✓	✓	✓	✓	✓	✓

Note: (a) Huang, Gao, et al. (2018) define artistic selection as the viewpoint that maximizes the projection of the actor on the image; (b) Bonatti et al. (2018) localize the actor visually only for control of the camera gimbal, but use GPS to obtain the actor's position in global coordinates for planning; (c) Cells marked with "Actor" for occlusion and obstacle avoidance mean that those approaches only take into account the actors in the scene as ellipsoidal obstacles, and disregard other objects.

3.3 | Making artistic choices autonomously

A common theme behind all the work presented so far is that a user must always specify which kind of output they expect from the system in terms of artistic behavior. This behavior is generally expressed in terms of the set of parameters Ω_{art} , and relates to different shot types, camera angles and angular speeds, type of actor framing, and so forth. If one wishes to autonomously specify artistic choices, two main points are needed: a proper definition of a metric for the artistic quality of a scene, and a decision-making agent which takes actions that maximize this quality metric, as explained in Equation (2).

Several works explore the idea of learning a beauty or artistic quality metric directly from data. Karpathy (2015) learns a measure for the quality of *selfies*; Fang and Zhang (2017) learn how to generate professional landscape photographs; Gatys, Ecker, and Bethge (2016) learn how to transfer image styles from paintings to photographs.

On the action generation side, we find works that have exploited deep RL (Mnih et al., 2015) to train models that follow human-specified behaviors. Closest to our work, Christiano et al. (2017) learn behaviors for which hand-crafted rewards are hard to specify, but which humans find easy to evaluate.

Our work, as described in Section 8, brings together ideas from all the aforementioned areas to create a generative model for shot type selection in aerial filming drones which maximizes an artistic quality metric.

3.4 | Online environment mapping

Dealing with imperfect representations of the world becomes a bottleneck for viewpoint optimization in physical environments. As the world is sensed online, it is usually incrementally mapped using

voxel occupancy maps (Thrun, Burgard, & Fox, 2005). To evaluate a viewpoint, methods typically ray-cast on such maps, which can be very expensive (Charrow et al., 2015; Isler, Sabzevari, Delmerico, & Scaramuzza, 2016). Recent advances in mapping have led to better representations that can incrementally compute the *truncated signed distance field* (TSDF; Klingensmith, Dryanovski, Srinivasa, & Xiao, 2015; Newcombe et al., 2011), that is, return the distance and gradient to nearest object surface for a query. TSDFs are a suitable abstraction layer for planning approaches and have already been used to efficiently compute collision-free trajectories for UAVs (Cover, Choudhury, Scherer, & Singh, 2013; Oleynikova, Taylor, Fehr, Nieto, & Siegwart, 2016).

3.5 | Visual target state estimation

Accurate object state estimation with monocular cameras is critical for many robot applications, including autonomous aerial filming. Two key problems in target state estimation include detecting objects and their orientation.

Deep learning-based techniques have achieved remarkable progress in the area of 2D object detection, such as You Only Look Once (YOLO; Redmon, Divvala, Girshick, & Farhadi, 2016), Single Shot Detector (SSD; W. Liu, Anguelov, et al., 2016), and Faster R-CNN method (Ren, He, Girshick, & Sun, 2015). These methods use convolutional neural networks (CNNs) for bounding box regression and category classification. They require powerful graphics processing units (GPUs), and cannot achieve real-time performance when deployed to the onboard platform. Another problem with off-the-shelf models trained on open data sets is that they do not generalize well to the areal filming scenario due to mismatches in data distribution due to angles, lighting, distances to actor and motion blur. Later in Section 5, we present our approach for obtaining a real-time object detector for our application.

Another key problem in the actor state estimation for aerial cinematography is estimating the heading direction of objects in the scene. Heading direction estimation (HDE) has been widely studied especially in the context of humans and cars as target objects. There have been approaches that attach sensors including inertial sensors and GPS to the target object to obtain the object's (Deng, Si, Qu, Liu, & Na, 2017; D. Liu, Pei, et al., 2016; Vista, Lee, & Chong, 2015) heading direction. While these sensors provide reliable and accurate estimation, it is highly undesirable for the target actor to carry these extra sensors. Thus, we primarily focus on vision-based approaches for our work that do not require the actor to carry any additional equipment.

In the context of HDE using visual input, there have been approaches based on classical machine learning techniques. Based on a probabilistic framework, Flohr, Dumitru-Guzu, Kooij, and Gavrila (2015) present a joint pedestrian head and body orientation estimation method, in which they design a HOG-based linear support vector machines pedestrian model. Learning features directly from data rather than hand-crafting them has proven more successful, especially in the domain of computer vision. We, therefore, leverage

learning-based approaches that ensure superior generalizability and improved robustness.

Deep learning-based approaches have been successfully applied to the area of 2D pose estimation (Cao, Simon, Wei, & Sheikh, 2017; Toshev & Szegedy, 2014) which is a related problem. However, the 3D heading direction cannot be trivially recovered from 2D points because the keypoint's depth remains undefined and ambiguous. Also, these approaches are primarily focused on humans and do not address other objects including cars.

There are fewer large-scale data sets for 3D pose estimation (Geiger, Lenz, Stiller, & Urtasun, 2013; Ionescu, Papava, Olaru, & Sminchisescu, 2014; W. Liu et al., 2013; Raman, Sa, Majhi, & Bakshi, 2016) and the existing ones generalize poorly to our aerial filming task, again due to mismatch in the data distribution. Thus, we look for approaches that can be applied in a limited labeled data setting. The limited data set constraint is common in many robotics applications, where the cost of acquiring and labeling data is high. Semisupervised learning (SSL) is an active research area in this domain. However, most of the existing SSL works are primarily focused on classification problems (Dai, Yang, Yang, Cohen, & Salakhutdinov, 2017; Hoffer & Ailon, 2016; Rasmus, Berglund, Honkala, Valpola, & Raiko, 2015; Weston, Ratle, Mobahi, & Collobert, 2012), which assume that different classes are separated by a low-density area and easy to separate in high dimensional space. This assumption is not directly applicable to regression problems.

In the context of cinematography, temporal continuity can be leveraged to formulate a semisupervised regression problem. Mobahi, Collobert, and Weston, (2009) developed one of the first approaches to exploit temporal continuity in the context of deep convolutional neural networks. The authors use video temporal continuity over the unlabeled data as a pseudosupervisory signal and demonstrate that this additional signal can improve object recognition in videos from the COIL-100 data set (Nene, Nayar, & Murase, 1996). There are other works that learn feature representations by exploiting temporal continuity (Goroshin, Bruna, Tompson, Eigen, & LeCun, 2015; Srivastava, Mansimov, & Salakhudinov, 2015; Stavens & Thrun, 2010; X. Wang & Gupta, 2015; Zou, Zhu, Yu, & Ng, 2012). Zou et al. (2012) included the video temporal constraints in an autoencoder framework and learned invariant features across frames. X. Wang and Gupta (2015) designed a Siamese-triplet network that can be trained in an unsupervised manner with a large amount of video data and showed that the unsupervised visual representation can achieve competitive performance on various tasks, compared to its ImageNet-supervised counterpart. Inspired by these approaches, our recent work (W. Wang et al., 2019) aims to improve the learning of a regression model from a small labeled data set by leveraging unlabeled video sequences to enforce temporally smooth output predictions.

After the target's location and heading direction is estimated on the image plane, we can project it onto the world coordinates and use different methods to estimate the actor's future motion. Motion forecast methods can range from filtering methods such as Kalman filters and extended Kalman filters (Thrun et al., 2005), which are

based solely on the actor's dynamics, to more complex methods that take into account environmental features as well. As an example of the latter, Urmson et al. (2008) use traditional motion planner with hand-crafted cost functions for navigation among obstacles, and Zhang, Wang, Bonatti, Maturana, and Scherer (2018) use deep inverse RL to predict the future trajectory distribution vehicles among obstacles.

4 | SYSTEM OVERVIEW

In this section, we detail the design hypotheses (Section 4.1) that influenced the system architecture layout (Section 4.2), as well as our hardware (Section 4.3) and simulation (Section 4.4) platforms.

4.1 | Design hypotheses

Given the application challenges (Section 1.1) and problem definition (Section 2), we defined three key hypotheses to guide the layout of the system architecture for the autonomous aerial cinematography task. These hypotheses serve as high-level principles for our choice of subsystems, sensors, and hardware. We evaluate the hypotheses later in Section 9, where we detail our simulation and field experiments.

Hyp. 1. *Onboard sensors can provide sufficient information for good cinematography performance.* This is a fundamental assumption and a

necessary condition for the development of real-world aerial cinematography systems that do not rely on ground-truth data from off-board sensors. We hypothesize that our system can deal with noisy measurements and extract necessary actor and obstacle information for visual actor localization, mapping, and planning.

Hyp. 2. *Decoupling gimbal control from motion planning improves real-time performance and robustness to noisy actor measurements.* We assume that an independent 3-DOF camera pose controller can compensate for noisy actor measurements. We expect advantages in two subsystems: (a) the motion planner can operate faster and with a longer time horizon due to the reduced trajectory state space, and (b) visual tracking will be more precise because the controller uses direct image feedback instead of a noisy estimate of the actor's location. We use a gimballed camera with 3-DOF control, which is a reasonable requirement given today's UAV and camera technology.

Hyp. 3. *Analogous to the role of a movie director, the artistic intent subsystem should provide high-level guidelines for camera positioning, but not interfere directly on low-level controls.* We hypothesize that a hierarchical structure to guide artistic filming behavior employing high-level commands is preferable to an end-to-end low-level visuo-motor policy because: (a) it is easier to ensure overall system safety and stability by relying on more established motion planning techniques, and (b) it is more data-efficient and easier to train a high-level decision-making agent than an end-to-end low-level policy.

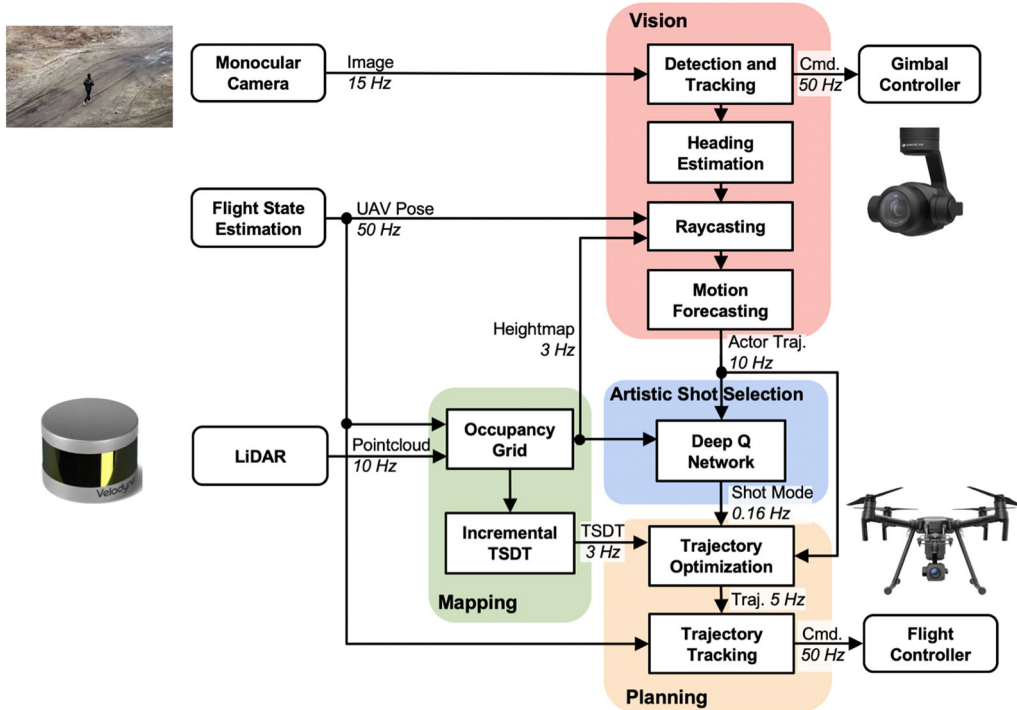


FIGURE 2 The system consists of four main modules running in parallel: Vision, mapping, planning, and artistic shot selection. The system takes in visual, LiDAR, and GPS inputs to output gimbal and flight controller commands [Color figure can be viewed at wileyonlinelibrary.com]

4.2 | System architecture

Taking into account the design hypotheses, we outline the software architecture in Figure 2. The system consists of four main modules: Vision, mapping, planning and artistic shot selection. The four modules run in parallel, taking in-camera, LiDAR and GPS inputs to output gimbal and flight controller commands for the UAV platform.

4.2.1 | Vision (Section 5)

The module takes in monocular images to compute a predicted actor trajectory for the Shot Selection and Planning Module. Following Hyp. 2, the vision module also controls the camera gimbal independently of the planning module.

4.2.2 | Mapping (Section 6)

The module registers the accumulated LiDAR point cloud and outputs different environment representations: obstacle height map for ray-casting and shot selection, and truncated signed distance transform (TSDF) map for the motion planner.

4.2.3 | Artistic shot selection (Section 8)

Following Hyp. 3 the module acts as an *artistic movie director* and defines high-level inputs for the motion planner defining the most esthetic shot type (left, right, front, and back) for a given scene context, composed of actor trajectory and obstacle locations.

4.2.4 | Planning (Section 7)

The planning module takes in the predicted actor trajectory, TSDF map, and the desired artistic shot mode to compute

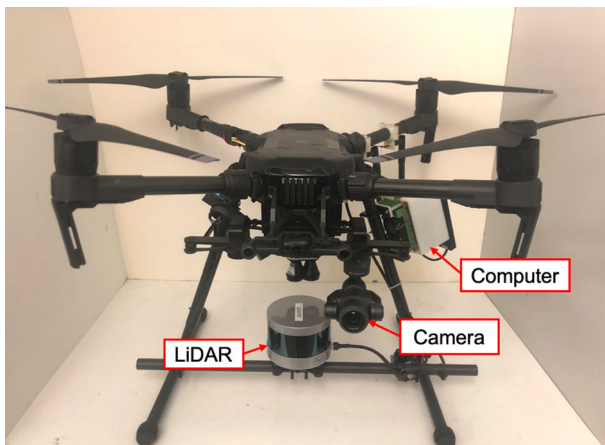


FIGURE 3 System hardware: DJI M210 drone equipped with Nvidia TX2 computer, Velodyne VLP-16 Puck Lite LiDAR and Zenmuse X4S camera gimbal [Color figure can be viewed at wileyonlinelibrary.com]

TABLE 2 System and payload weights

Component	Weight (kg)
DJI M210	2.80
DJI Zenmuse X4S	0.25
DJI TB 50 batteries × 2	1.04
NVIDIA TX2 w/cARRIER board	0.30
VLP-16 Lite	0.59
Structure modifications	0.63
Cables and connectors	0.28
Total	5.89 ≤ 6.14 (maximum takeoff weight ^a)

^a<https://www.dji.com/products/compare-m200-series>

a trajectory that balances safety, smoothness, shot quality, and occlusion avoidance. Using the UAV pose estimate, the module outputs velocity commands for the UAV to track the computed trajectory.

4.3 | Hardware

Our base platform is the DJI M210 quadcopter, shown in Figure 3. The UAV fuses GPS, IMU, and compass for state estimation, which can be accessed via DJI's SDK. The M210 has a maximum payload capacity of 2.30 kg¹, which limits our choice of batteries and onboard computers and sensors.

Our payload is composed of (weights are summarized in Table 2):

- DJI TB50 batteries, with a maximum flight time of 13 min at full payload;
- DJI Zenmuse X4S gimbaled camera, whose 3-axis gimbal can be controlled independently of the UAV's motion with angular precision of ±0.01°, and counts with a vibration-dampening structure. The camera records high-resolution videos, up to 4 K at 60 FPS;
- NVIDIA Jetson TX2 with Astro carrier board. 8 GB of RAM, six CPU cores and 256 GPU cores for onboard computation;
- Velodyne Puck VLP-16 Lite LiDAR, with ±15° vertical field of view and 100 m max range.

4.4 | Photo-realistic simulation platform

We use the Microsoft AirSim simulation platform (Shah, Dey, Lovett, & Kapoor, 2018) to test our framework and to collect training data for the shot selection module, as explained in detail in Section 8. AirSim offers a high-fidelity visual and physical simulation for quadrotors and actors (such as humans and cars), as shown in Figure 4. We built a custom ROS (Quigley et al., 2009) interface for the simulator, so that our system can switch between the simulation and the real drone seamlessly. All nodes from the system

¹<https://www.dji.com/products/compare-m200-series>

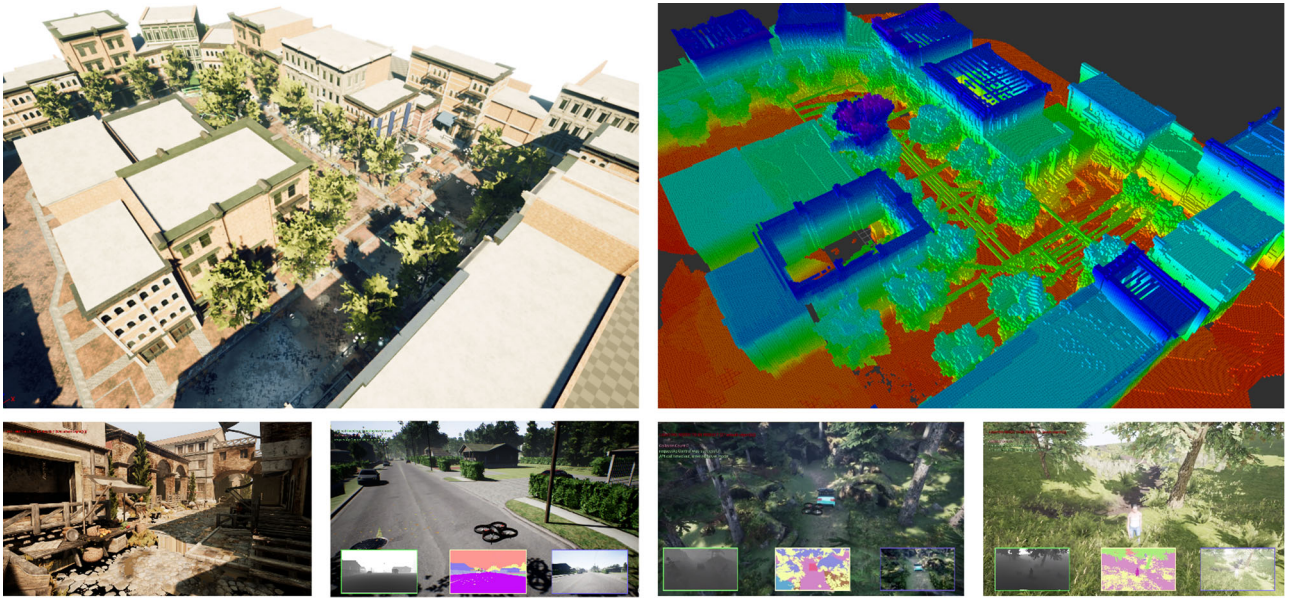


FIGURE 4 Simulation platform: AirSim combines a physics engine with photorealistic renderings of various environments and actors (human and vehicles). Here we show the urban and forest environments we used for testing our framework. We build a point cloud and an occupancy map in the simulation. The simulation provides ground truth data for the actor's pose, which is used to evaluate the performance of the vision pipeline [Color figure can be viewed at [wileyonlinelibrary.com](#)]

architecture are written in C++ and Python languages, and communicate using the ROS framework.

5 | VISUAL ACTOR LOCALIZATION AND HEADING ESTIMATION

The vision module is responsible for two critical roles in the system: to estimate the actor's future trajectory and to control the camera gimbal to keep the actor within the frame. Figure 5 details the four main submodules: actor detection and tracking, heading direction angle estimation, global position ray-casting, and finally a filtering stage for trajectory forecasting. Next, we detail each submodule.

5.1 | Detection and tracking

As we discussed in Section 3, the state-of-the-art object detection methods require large computational resources, which are not available on our onboard platform, and do not perform well in our scenario due to the data distribution mismatch. Therefore, we develop two solutions: first, we build a custom network structure and

train it on both the open and context-specific data sets to improve speed and accuracy; second, we combine the object detector with a real-time tracker for stable performance.

The deep learning-based object detectors are composed of a feature extractor followed by a classifier or regressor. Different feature extractors could be used in each detector to balance efficiency and accuracy. Since the onboard embedded GPU is less powerful, we can only afford feature extractor with relatively fewer layers. We compare several lightweight publicly available trained models for people detection and car detection.

Due to good real-time inference speed and low memory usage, we combine the MobileNet (Howard et al., 2017) for feature extraction and the Faster-RCNN (Ren et al., 2015) architecture. Our feature extractor consists of 11 depth-wise convolutional modules, which contain 22 convolutional layers. Following the Faster-RCNN structure, the extracted feature then goes to a two-stage detector, namely a region proposal stage and a bounding box regression and a classification stage. While the size of the original Faster-RCNN architecture with VGG is 548 MB, our custom network's is 39 MB, with an average inference time of 300 ms.

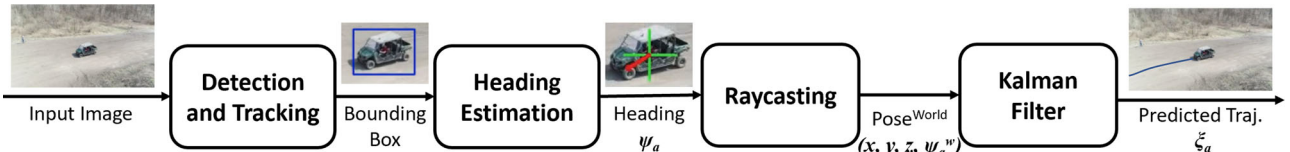


FIGURE 5 Vision subsystem. We detect and track the actor's bounding box, estimate its heading, and project its pose to world coordinates. A Kalman filter predicts the actor's forecasted trajectory ξ_a [Color figure can be viewed at [wileyonlinelibrary.com](#)]

The distribution of images in the aerial filming task differs significantly from the usual images found in openly accessible data sets, due to highly variable relative yaw and tilt angles to the actors, large distances, varying lighting conditions, and heavy motion blur. Figure 6 displays examples of challenging situations faced in the aerial cinematography problem. Therefore, we trained our network with images from two sources: a custom data set of 120 challenging images collected from field experiments, and images from the COCO (Lin et al., 2014) data set, in a 1:10 ratio. We limited the detection categories only to person, car, bicycle, and motorcycle, which are object types that commonly appear as actors in aerial filming.

The detection module receives the main camera's monocular image as inputs and outputs a bounding box. We use this initial bounding box to initialize a template tracking process and reinitialize detection whenever the tracker's confidence falls below acceptable limits. We adopt this approach, as opposed to detecting the actor in every image frame, because detection is a computationally heavy process, and the high rate of template tracking provides more stable measurements for subsequent calculations. We use Kernelized Correlation Filters (Henriques, Caseiro, Martins, & Batista, 2015) to track the template over the next incoming frames.

As mentioned in Section 4, we actively control camera gimbal independently of the UAV's motion to maintain visibility of the target. We use a PD controller to frame the actor on the desired screen position, following the commanded artistic principles from the operator. Typically, the operator centers the target in the middle of the image space, or uses visual composition rules such as the rule of thirds (Bowen & Thompson, 2013), as seen on Figure 7.

5.2 | Heading estimation

When filming a moving actor, HDE plays a central role in motion planning. Using the actor's heading information, the UAV can position itself within the desired shot type determined by the user's artistic objectives, for example, back, front, left, and right-side shots, or within any other desired relative yaw angle.

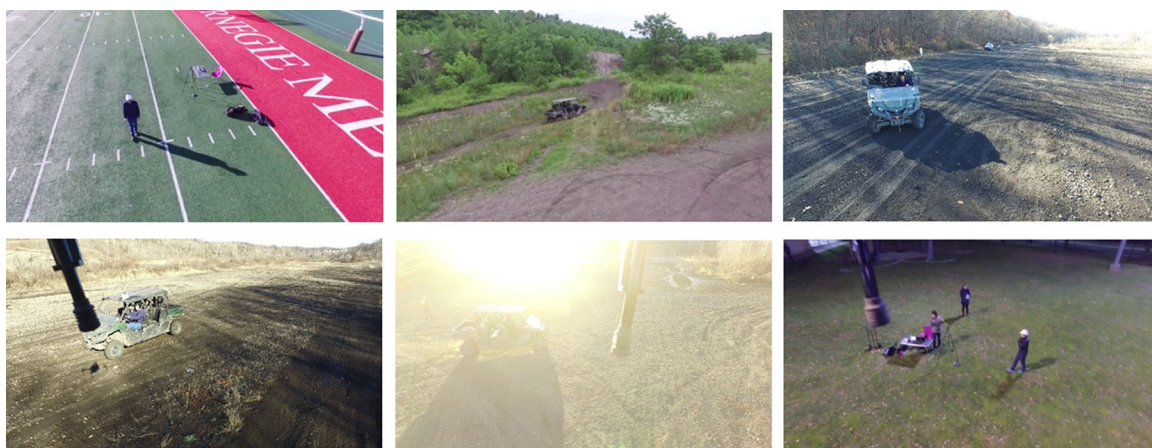


FIGURE 6 Examples of challenging images for actor detection in the aerial filming task. Large relative tilt angles to the ground, variable lighting, large distance to actor, and heavy motion blur make bounding box detection harder than in images from open data sets [Color figure can be viewed at [wileyonlinelibrary.com](#)]



FIGURE 7 Desired screen position of the actor projection, defined by parameters: $sp_x, sp_y \in [0, 1]$. Typically the user uses one-third of the screen to set the actor's position or centers the actor on the frame (Bowen & Thompson, 2013) [Color figure can be viewed at [wileyonlinelibrary.com](#)]

Estimating the heading of people and objects is also an active research problem in many other applications, such as pedestrian collision risk analysis (Tian et al., 2014), human-robot interaction (Vázquez, Steinfeld, & Hudson, 2015) and activity forecasting (Kitani, Ziebart, Bagnell, & Hebert, 2012). Similar to challenges in bounding box detection, models obtained in other data sets do not easily generalize to the aerial filming task, due to a mismatch in the types of images from data sets to our application. In addition, when the trained model is deployed on the UAV, errors are compounded because the HDE relies on an imperfect object detection module, increasing the mismatch (Geiger et al., 2013; Ristani, Solera, Zou, Cucchiara, & Tomasi, 2016).

No current data set satisfies our needs for aerial HDE, creating the need for us to create a custom labeled data set for our application. As most deep learning approaches, training a network is a data-intensive process, and manually labeling a large enough data set for conventional supervised learning is a laborious and expensive task. The process is further complicated as multiple actor types such as people, cars, and bicycles can appear in footages.

These constraints motivated us to formulate a novel semisupervised algorithm for the HDE problem (W. Wang et al., 2019). To drastically reduce the quantity of labeled data, we leverage temporal continuity in video sequences as an unsupervised signal to regularize the model and achieve better generalization. We apply the semisupervised algorithm in both training and testing phases, drastically increasing inference performance, and show that by leveraging unlabeled sequences, the amount of labeled data required can be significantly reduced.

5.2.1 | Defining the loss for temporal continuity

We define the pose of the actor as a vector $[x, y, z, \psi_a^w]$ on the ground surface. To estimate the actor's heading direction in the world frame ψ_a^w , we first predict the actor's heading ψ_a in the image frame, as shown in Figure 8. Once ψ_a is estimated, we project this direction onto the world frame coordinates using the camera's intrinsic and extrinsic matrices.

The HDE module outputs the estimated heading angle ψ_a in image space. Since ψ_a is ambiguously defined at the frontier between $-\pi$ and π , we define the inference as a regression problem that outputs two continuous values: $[\cos(\psi_a), \sin(\psi_a)]$. This avoids model instabilities during training and inference.

We assume access to a relatively small labeled data set $D = \{(x_i, y_i)\}_{i=0}^n$, where x_i denotes input image, and $y_i = [\cos(\psi_i), \sin(\psi_i)]$ denotes the angle label. In addition, we assume access to a large unlabeled sequential data set $U = \{q_j\}_{j=0}^m$, where $q_j = \{x_0, x_1, \dots, x_t\}$ is a sequence of temporally continuous image data.

The HDE module's main objective is to approximate a function $y = f(x)$, that minimizes the regression loss on the labeled data $\sum_{(x, y) \in D} L_f(x_i, y_i) = \sum_{(x, y) \in D} \|y_i - f(x_i)\|^2$. One intuitive way to leverage unlabeled data is to add a constraint that the output of the model should not have large discrepancies over a consecutive input sequence. Therefore, we train the model to jointly minimize the labeled loss L_f and some continuity loss L_u . We minimize the combined loss:

$$L_{\text{tot}} = \min \sum_{(x_i, y_i) \in D} L_f(x_i, y_i) + \lambda \sum_{q_j \in U} L_u(q_j). \quad (3)$$

We define the unsupervised loss using the idea that samples closer in time should have smaller differences in angles than



FIGURE 8 Example of actor bounding boxes and their respective heading angles ψ_a in image space. Given the images, our objective is to predict the heading direction, shown as red arrows [Color figure can be viewed at wileyonlinelibrary.com]

samples further away in time. A similar continuity loss is also used by X. Wang and Gupta (2015) when training an unsupervised feature extractor:

$$\begin{aligned} L_u(q_u) &= \sum_{x_1, x_2, x_3} \max[0, D(x_1, x_2; f) - D(x_1, x_3; f)], \\ \text{where } D(x_1, x_2; f) &= \|f(x_1) - f(x_2)\|_2, \\ \text{and } x_1, x_2, x_3 &\in q_u \end{aligned} \quad (4)$$

5.2.2 | Network structure

For lower memory usage and faster inference time in the onboard computer, we design a compact CNN architecture based on MobileNet (Howard et al., 2017). The input to the network is a cropped image of the target's bounding box, outputted by the detection and tracking modules. The cropped image is padded to a square shape and resized to 192×192 pixels. After the 10 group-wise and point-wise convolutional blocks from the original MobileNet architecture, we add another convolutional layer and a fully connected layer that output two values representing the cosine and sine values of the angle. Figure 9 illustrates the architecture.

During each training iteration, one shuffled batch of labeled data and one sequence of unlabeled data are passed through the network. The labeled loss and unlabeled losses are computed and back-propagated through the network.

5.2.3 | Cross-data set semisupervised fine-tuning

Due to data distribution mismatch between the aerial cinematography task and open data sets, we train our network on a combination of images from both sources. Later in Section 9.2 we evaluate the impact of fine-tuning the training process with unsupervised videos from our application.

5.3 | Ray-casting

The ray-casting module convert the detection/tracking and HDE results from image space to coordinates and heading in the world frame $[x, y, z, \psi_a^w]$. Given the actor's bounding box, we project its center-bottom point onto a height map of the terrain, provided by

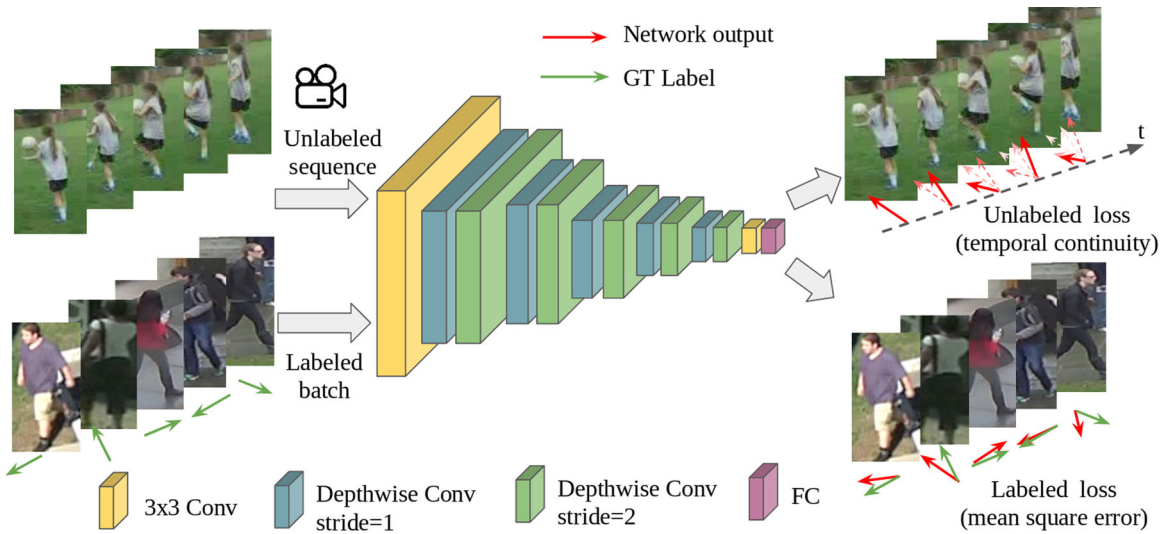


FIGURE 9 Our network architecture for predicting the actor's heading direction. We use a Mobilenet-based feature extractor followed by a convolutional layer and a fully connected layer to regress to angular values. The network is trained using both labeled and unsupervised losses [Color figure can be viewed at [wileyonlinelibrary.com](#)]

the mapping module. The intersection of this line with the heightmap provides the $[x, y, z]$ location of the actor.

Assuming that the camera gimbal's roll angle is fixed at zero degrees by the active gimbal controller, we can directly obtain the actor's heading direction on the world frame ψ_a^w by transforming the heading ψ from the image space with the camera's extrinsic matrix in world coordinates (Figure 10).

5.4 | Motion forecasting

Given a sequence of actor poses in the world coordinates, we estimate the actor's future trajectory based on motion models. The motion planner later uses the forecast to plan nonmyopically over long time horizons.

We use two different motion models depending on the actor types. For people, we apply a linear Kalman filter with a two-dimensional motion model. Since a person's movement direction can change drastically, we use no kinematic constraints applied to the motion model,

and just assume constant velocity. We assume no control inputs for state $[x, y, \dot{x}, \dot{y}]$ in the prediction step, and use the next measurement of $[x, y, z]$ in the correction step. When forecasting the motion of cars and bicycles we apply an extended Kalman filter with a kinematic bicycle model. For both cases, we use a 10 s horizon for prediction.

6 | ONLINE ENVIRONMENT MAPPING

As explained in Section 2, the motion planner requires signed distance values \mathcal{M} to solve the optimization problem that results in the final UAV trajectory. The main role of the mapping subsystem described here is to register LiDAR points from the onboard sensor, update the occupancy grid \mathcal{G} , and incrementally update the signed distance \mathcal{M} .

6.1 | LiDAR registration

During our filming operation, we receive approximately 300,000 points per second from the laser sensor mounted at the bottom of the aircraft. We register the points in the world coordinate system using a rigid body transform between the sensor and the aircraft plus the UAV's state estimation, which fuses GPS, barometer, internal IMUs and accelerometers. For each point, we also store the corresponding sensor coordinate, which is used for the occupancy grid update.

LiDAR points can be categorized either as hits, which represent successful laser returns within the maximum range of 100 m, or as misses, which represent returns that are either nonexistent, beyond the maximum range, or below a minimum sensor range. We filter all expected misses caused by reflections from the aircraft's own structure. Finally, we probabilistically update all voxels from \mathcal{G} between the sensor and its LiDAR returns, as described in Section 6.2.

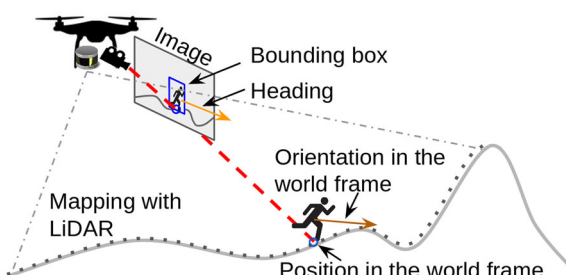


FIGURE 10 Ray-casting module uses the actor's bounding box, estimated heading angle, environment height map, and camera matrices to obtain pose of the actor in the world frame $[x, y, z, \psi_a^w]$ [Color figure can be viewed at [wileyonlinelibrary.com](#)]

6.2 | Occupancy grid update

The mapping subsystem holds a rectangular grid that stores the likelihood that any cell in space is occupied. In this study, we use a grid size of $250 \times 250 \times 100$ m, with 1 m square voxels that store an 8-bit integer value between 0 and 255 as the occupancy probability, where 0 is the limit for a fully free cell, and 255 is the limit for a fully occupied cell. All cells are initialized as *unknown*, with value of 127.

Algorithm 1 covers the grid update process. The inputs to the algorithm are the sensor position p_{sensor} , the LiDAR point p_{point} , and a flag *is_hit* that indicates whether the point is a hit or miss. The endpoint voxel of a hit will be updated with log-odds value l_{occ} , and all cells in between sensor and endpoint will be updated by subtracting value l_{free} . We assume that all misses are returned as points at the maximum sensor range, and in this case, only the cells between endpoint and sensor are updated l_{free} .

As seen in Algorithm 1, all voxel state changes to *occupied* or *free* are stored in lists $V_{\text{occ}}^{\text{change}}$ and $V_{\text{free}}^{\text{change}}$. State changes are used for the signed distance update, as explained in Section 6.3.

Algorithm 1: Update \mathcal{G} (p_{sensor} , p_{point} , *is_hit*)

```

1 Initialize  $V_{\text{occ}}^{\text{change}}$ ,  $V_{\text{free}}^{\text{change}}$  > list of changed voxels
2 Initialize  $l_{\text{free}}$ ,  $l_{\text{occ}}$  > log-odds probabilistic updates
3 for each voxel  $v$  between  $p_{\text{sensor}}$  and  $p_{\text{point}}$  do
4    $v \leftarrow v - l_{\text{free}}$ ;
5   if  $v$  was occupied or unknown and now is free then
6     Append( $v$ ,  $V_{\text{free}}^{\text{change}}$ );
7     for each unknown neighbor  $v_{\text{unk}}$  of  $v$  do
8       Append( $v_{\text{unk}}$ ,  $V_{\text{occ}}^{\text{change}}$ )
9     end
10    end
11    if  $v$  is the endpoint and is_hit is true then
12       $v \leftarrow v + l_{\text{occ}}$ ;
13      if  $v$  was free or unknown and now is occupied then
14        Append( $v$ ,  $V_{\text{occ}}^{\text{change}}$ )
15      end
16    end
17  end
18 return  $V_{\text{occ}}^{\text{change}}$ ,  $V_{\text{free}}^{\text{change}}$ 
```

6.3 | Incremental distance transform update

We use the list of voxel state changes as input to an algorithm, modified from Cover et al. (2013), that calculates an incremental TSDT (iTSDT), stored in \mathcal{M} . The original algorithm described by Cover et al. (2013) initializes all voxels in \mathcal{M} as free, and as voxel changes arrive in sets $V_{\text{occ}}^{\text{change}}$ and $V_{\text{free}}^{\text{change}}$, it incrementally updates the distance of each free voxel to the closest occupied voxel using an efficient wavefront expansion technique within some limit (therefore truncated).

Our problem, however, requires a *signed* version of the DT, where the *inside* and *outside* of obstacles must be identified and given opposite signs (details of this requirement are given in the description of the occlusion cost function detailed in Section 7). The concept of regions inside and outside of obstacles cannot be

captured by the original algorithm, which provides only a iTDT (with no sign). Therefore, we introduced two important modifications.

6.3.1 | Using the borders of obstacles

The original algorithm uses only the occupied cells of \mathcal{G} , which are incrementally pushed into \mathcal{M} using set $V_{\text{occ}}^{\text{change}}$. We, instead, define the concept of *obstacle border* cells, and push them incrementally as $V_{\text{occ}}^{\text{change}}$.

Let v_{border} be an obstacle border voxel, and V_{border} be the set of all border voxels in the environment. We define v_{border} as any voxel that is either a direct hit from the LiDAR (lines 13–15 of Algorithm 1), or as any *unknown* voxel that is a neighbor of a *free* voxel (lines 5–9 of Algorithm 1). In other words, the set V_{border} will represent all cells that separate the known free space from unknown space in the map, whether this unknown space is part of cells inside an obstacle or cells that are actually free but just have not yet been cleared by the LiDAR.

By incrementally pushing $V_{\text{occ}}^{\text{change}}$ and $V_{\text{free}}^{\text{change}}$ into \mathcal{M} , its data structure will maintain the current set of border cells V_{border} . By using the same algorithm described in Cover et al. (2013) but now with this distinct type of data input, we can obtain the distance of any voxel in \mathcal{M} to the closest obstacle border. One more step is required to obtain the sign of this distance.

6.3.2 | Querying \mathcal{G} for the sign

The data structure of \mathcal{M} only stores the distance of each cell to the nearest obstacle border. Therefore we query the value of \mathcal{G} to attribute the sign of the iTSDT, marking free voxels as positive, and unknown or occupied voxels as negative (Figure 11).

6.4 | Building a height map

Despite keeping a full 3D map structure as the representation used for planning (Section 7), we also incrementally build a height map of

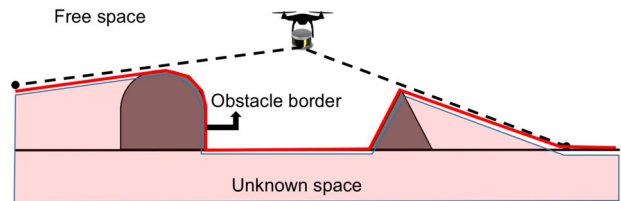


FIGURE 11 Diagram with our obstacle representation. Unknown voxels (red shade) are either inside of obstacles, or in zones occluded from the sensor's field of view. The red line displays the obstacle border, which is at the interface between LiDAR hits and free space, and at the interface between unknown and free space. In this conceptual figure, we assume the sensor to be omnidirectional, so the ground and obstacles below aircraft were captured as hits; however, in practice the sensor has a field of view limitations [Color figure can be viewed at wileyonlinelibrary.com]

the environment that is used for both the ray-casting procedure when finding the actor position in world coordinates (Section 5), and for the online learned artistic shot type selection procedure (Section 8).

The height map is a 2D array where the value of each cell corresponds to a moving average of the height of the LiDAR hits that arrive in each position. All cells are initialized with 0 m of height, relative to the world coordinate frame, which is taken from the UAV's takeoff position. An example height map is shown in Figure 12.

7 | MOTION PLANNING

The motion planner's objective is to calculate trajectories for the UAV to film the moving actor. Next we detail the definition of our trajectory, cost functions, the trajectory optimization algorithm, and implementation details.

7.1 | UAV trajectory definition

Recall Section 2, where we defined $\xi_q(t) : [0, t_f] \rightarrow \mathbb{R}^3 \times SO(2)$ as the UAV trajectory and $\xi_a(t) : [0, t_f] \rightarrow \mathbb{R}^3 \times SO(2)$ as the actor trajectory, where $\xi_q(t) = \{x_q(t), y_q(t), z_q(t), \psi_q(t)\}$ and $\xi_a(t) = \{x_a(t), y_a(t), z_a(t), \psi_a(t)\}$. High-frequency measurements of the actor's current position generate the actor's motion forecast $\xi_a(t)$ in the vision module (Section 5.4), and it is the motion planner's objective to output the UAV trajectory $\xi_q(t)$.

Since the gimbal controller can position the camera independently of the UAV's body motion, we purposefully decouple the UAV's body heading $\psi(t)$ from the main motion planning algorithm. We set $\psi_q(t)$ to always point from $\xi_q(t)$ toward $\xi_a(t)$ at all times, as seen in Equation (5).

$$\psi_q(t) = \text{atan2}(y_a(t) - y_q(t), x_a(t) - x_q(t)). \quad (5)$$

This assumption significantly reduces the complexity of the planning problem by removing four degrees of freedom (three from the camera and one from the UAV's heading), and improves filming

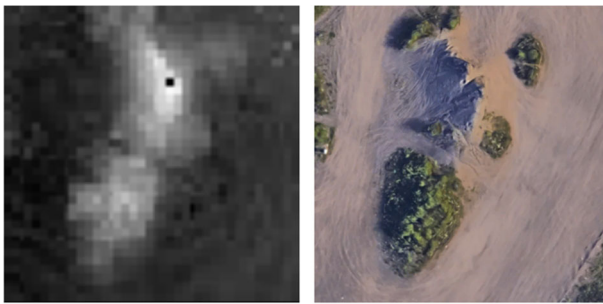


FIGURE 12 The left figure shows the height map accumulated overflight over a small mountain. The color scale goes from 0 (-10 m) to 255 ($+10$ m), where the zero reference of 127 is taken at the unmanned aerial vehicles initial takeoff height. The right figure is the top-down view of the mountain of the same place [Color figure can be viewed at wileyonlinelibrary.com]

performance because the camera can be controlled directly from image feedback, without the accumulation of errors from the ray-casting module (Section 5).

Now, let $\xi_q(t)$ represent the UAV's trajectory in a continuous time-parametrized form, and let ξ_q represent the same trajectory in a finite discrete form, with total time length t_f . Let point p_0 represents the contour conditions of the beginning of the trajectory. ξ_q contains a total of $n - 1$ waypoints of the form p_i , where $i = 1, \dots, n - 1$, as shown in Equation (6).

$$\xi_q = \begin{bmatrix} p_1 \\ p_2 \\ \vdots \\ p_{n-1} \end{bmatrix} = \begin{bmatrix} p_{1x} & p_{1y} & p_{1z} \\ p_{2x} & p_{2y} & p_{2z} \\ \vdots & \vdots & \vdots \\ p_{n-1x} & p_{n-1y} & p_{n-1z} \end{bmatrix}. \quad (6)$$

7.2 | Planner requirements

As explained in Section 2, in a generic aerial filming framework we want trajectories which are smooth (J_{smooth}), capture high-quality viewpoints (J_{shot}), avoid occlusions (J_{occ}) and keep the UAV safe (J_{obs}). Each objective can then be encoded in a separate cost function, and the motion planner's objective is to find the trajectory that minimizes the overall cost, assumed to be a linear combination of individual cost functions, subject to the initial condition constraints. For the sake of completeness, we repeat Equation (1) below as Equation (7):

$$J(\xi_q) = [1 \ \lambda_1 \ \lambda_2 \ \lambda_3] \begin{bmatrix} J_{\text{smooth}}(\xi_q) \\ J_{\text{obs}}(\xi_q, M) \\ J_{\text{occ}}(\xi_q, \xi_a, M) \\ J_{\text{shot}}(\xi_q, \xi_a, \Omega_{\text{art}}) \end{bmatrix}, \quad (7)$$

$$\xi_q^* = \arg \min_{\xi_q} J(\xi_q), \quad \text{s.t. } \xi_q(0) = \{x_0, y_0, z_0, \psi_0\}.$$

Our choice of cost functions and planning is dictated by two main observations. First, filming requires the UAV to reason over a longer horizon than reactive approaches, usually in the order of ~ 10 s. The UAV not only has to avoid local obstacles such as small branches or light posts, but also consider how larger obstacles such as entire trees, buildings, and terrain elevations may affect image generation. Note that the horizons are limited by how accurate the actor prediction is. Second, filming requires a high planning frequency. The actor is dynamic, constantly changing direction and velocity. The map is continuously evolving based on sensor readings. Finally, since jerkiness in trajectories have a significant impact on video quality, the plans need to be smooth, free of large time discretization.

Based on these observations, we chose local trajectory optimization techniques to serve as the motion planner. Optimizations are fast and reason over a smooth continuous space of trajectories. In addition, locally optimal solutions are almost always of acceptable quality, and plans can be incrementally updated across planning cycles.

A popular optimization-based approach that addresses the aerial filming requisites is to cast the problem as an unconstrained cost optimization, and apply covariant gradient descent (Ratliff, Silver, &

Bagnell, 2009; Zucker et al., 2013). This is a quasi-Newton method, and requires that some of the objectives have analytic Hessians that are easy to invert and that are well-conditioned. With the use of first and second-order information about the problem, such methods exhibit fast convergence while being stable and computationally inexpensive. The use of such quasi-Newton methods requires a set of differentiable cost functions for each objective, which we detail next.

7.3 | Definition of cost functions

7.3.1 | Smoothness

We measure smoothness as the cumulative sum of n th order derivatives of the trajectory, following the rationale of Ratliff, Zucker, et al. (2009). Let D be a discrete difference operator. The smoothness cost is

$$J_{\text{smooth}}(\xi_q(t)) = \frac{1}{t_f} \frac{1}{2} \int_0^{t_f} \sum_{d=1}^{d_{\max}} \alpha_d (D^d \xi_q(t))^2 dt, \quad (8)$$

where α_d is a weight for different orders, and d_{\max} is the number of orders. In practice, we penalize derivatives up to the third order, setting $\alpha_d = 1$, $d_{\max} = 3$. Appendix expands upon this cost function and reformulates it in matrix form using auxiliary matrices A_{smooth} , b_{smooth} , and c_{smooth} . We state the cost, gradient and Hessian for completeness:

$$\begin{aligned} J_{\text{smooth}}(\xi_q) &= \frac{1}{2(n-1)} \text{Tr}(\xi_q^T A_{\text{smooth}} \xi_q + 2\xi_q^T b_{\text{smooth}} + c_{\text{smooth}}), \\ \nabla J_{\text{smooth}}(\xi_q) &= \frac{1}{(n-1)} (A_{\text{smooth}} \xi_q + b_{\text{smooth}}), \\ \nabla^2 J_{\text{smooth}}(\xi_q) &= \frac{1}{(n-1)} A_{\text{smooth}}. \end{aligned} \quad (9)$$

7.3.2 | Shot quality

First, we analytically define the artistic shot parameters. Based on cinematography literature (Arijon, 1976; Bowen & Thompson, 2013), we select a minimal set of parameters that compose most of the shots possible for single-actor, single-camera scenarios. We define Ω_{art} as a set

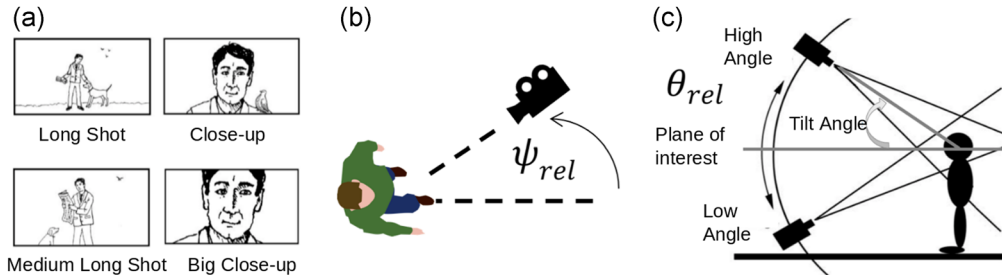


FIGURE 13 Shot parameters Ω_{art} for shot quality cost function, adapted from Bowen and Thompson (2013), (a) shot scale ρ corresponds to the size of the projection of the actor on the screen; (b) line of action-angle $\psi_{\text{rel}} \in [0, 2\pi]$; (c) tilt angle $\theta_{\text{rel}} \in [-\pi, \pi]$ [Color figure can be viewed at wileyonlinelibrary.com]

of three parameters: $\Omega_{\text{art}} = \{\rho, \psi_{\text{rel}}, \theta_{\text{rel}}\}$, where (a) ρ is the shot scale, which can be mapped to the distance between actor and camera, (b) ψ_{rel} is the relative yaw angle between actor and camera, and (c) θ_{rel} is the relative tilt angle between the actor's current height plane and the camera. Figure 13 depicts the components of Ω_{art} .

Given a set Ω_{art} , we can now define a desired cinematography path $\xi_{\text{shot}}(t)$:

$$\xi_{\text{shot}}(t) = \xi_a(t) + \rho \begin{bmatrix} \cos(\psi_a + \psi_{\text{rel}}) \sin(\theta_{\text{rel}}) \\ \sin(\psi_a + \psi_{\text{rel}}) \cos(\theta_{\text{rel}}) \\ \cos(\theta_{\text{rel}}) \end{bmatrix}, \quad (10)$$

Next, we can define an analytical expression for the shot quality cost function as the distance between the current camera trajectory and the desired cinematography path:

$$J_{\text{shot}}(\xi_q, \xi_a) = \frac{1}{t_f} \frac{1}{2} \int_0^{t_f} \|\xi_q(t) - \xi_{\text{shot}}(\xi_a(t))\|^2 dt. \quad (11)$$

Appendix expands upon this cost function and reformulates it in matrix form using auxiliary matrices A_{shot} , b_{shot} , and c_{shot} . Again, we state the cost, gradient, and Hessian for completeness:

$$\begin{aligned} J_{\text{shot}}(\xi_q, \xi_a) &= \frac{1}{2(n-1)} \text{Tr}(\xi_q^T A_{\text{shot}} \xi_q + 2\xi_q^T b_{\text{shot}} + c_{\text{shot}}), \\ \nabla J_{\text{shot}}(\xi_q) &= \frac{1}{(n-1)} (A_{\text{shot}} \xi_q + b_{\text{shot}}), \\ \nabla^2 J_{\text{shot}}(\xi_q) &= \frac{1}{(n-1)} A_{\text{shot}}. \end{aligned} \quad (12)$$

We note that although the artistic parameters of the shot quality cost described in this study are defined for single-actor single-camera scenarios, the extension of J_{shot} to multi-actor scenarios is trivial. It can be achieved by defining an artistic guideline ξ_{shot} using multi-actor parameters such as the angles with respect to the line of action (Bowen & Thompson, 2013), or geometric center of the targets. We detail more possible extensions of our work in Section 11.

7.3.3 | Safety

Given the online map \mathcal{G} , we can obtain the TSDT map $M: \mathbb{R}^3 \rightarrow \mathbb{R}$ as described in Section 6. Given a point p , we adopt the obstacle avoidance function from Zucker et al. (2013). This function linearly

penalizes the intersection with obstacles, and decays quadratically with distance, up to a threshold ϵ_{obs} :

$$c(p) = \begin{cases} -M(p) + \frac{1}{2}\epsilon_{\text{obs}} & M(p) < 0, \\ \frac{1}{2\epsilon_{\text{obs}}}(\mathcal{M}(p) - \epsilon_{\text{obs}})^2 & 0 < M(p) \leq \epsilon_{\text{obs}}, \\ 0 & \text{otherwise.} \end{cases} \quad (13)$$

Similarly to Zucker et al. (2013), define a safety cost function for the entire trajectory:

$$J_{\text{obs}}(\xi_q, M) = \int_{t=0}^{t_f} c(\xi_q(t)) \left| \frac{d}{dt} \xi_q(t) \right| dt. \quad (14)$$

We can differentiate J_{obs} with respect to a point at time t_i to obtain the cost gradient (note that $\hat{v} = \frac{v}{\|v\|}$ denotes a normalized vector):

$$\nabla J_{\text{obs}}(\xi_q(t_i), M) = \nabla J_{\text{obs}}(p_i, M) = |\dot{p}_i|_i [(I - \hat{p}_i \hat{p}_i^T) \nabla c(p_i) - c(p_i) \kappa],$$

where: $\kappa = \frac{1}{\|\dot{p}_i\|^2} (I - \hat{p}_i \hat{p}_i^T) \ddot{p}_i$. (15)

In practice, we use discrete derivatives to calculate M , the velocities \dot{p}_i , and accelerations \ddot{p}_i .

7.3.4 | Occlusion avoidance

Even though the concept of occlusion is binary, that is, we either have or do not have visibility of the actor, a major contribution of our past work (Bonatti et al., 2018) was to define a differentiable cost that expresses a viewpoint's occlusion intensity among arbitrary obstacle shapes. The fundamental idea behind this cost is that it measures along how much obstacle blockage the best possible camera viewpoints of ξ_q would go through, assuming the camera pointed directly at the actor's true position at all times. For illustration purposes, Figure 14 shows the concept of occlusion for motion in a 2D environment, even though our problem fully defined in 3D.

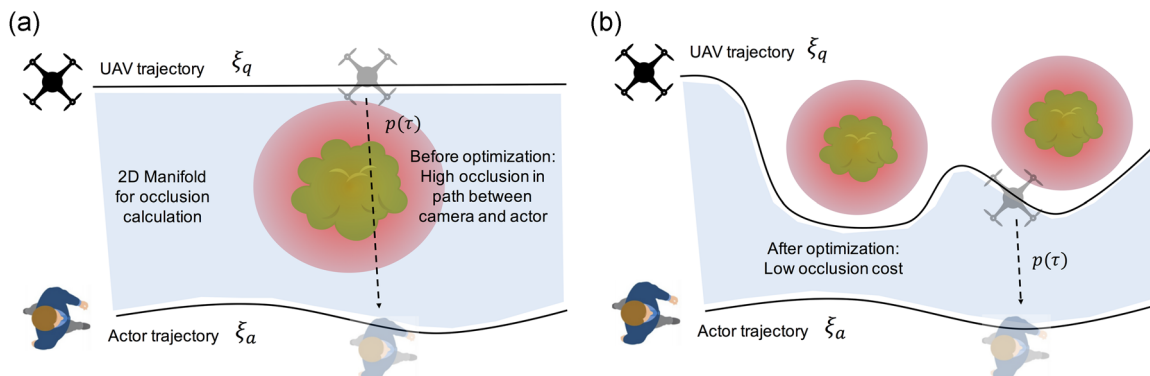


FIGURE 14 Occlusion cost representation. (a) For every pair of UAV-actor position, we integrate the penalization c on the signed distance field over a 2D manifold. (b) After optimization, occlusion gradients pull the UAV trajectory toward regions with full visibility of the actor. UAV, unmanned aerial vehicle [Color figure can be viewed at wileyonlinelibrary.com]

Mathematically, we define occlusion as the integral of the TSDT cost c over a 2D manifold connecting both trajectories ξ_q and ξ_a . The manifold is built by connecting each UAV-actor position pair at time t using the parametrized path $p(\tau)$, where $p(\tau=0) = \xi_q(t)$ and $p(\tau=1) = \xi_a(t)$:

$$J_{\text{occ}}(\xi_q, \xi_a, M) = \int_{t=0}^{t_f} \left(\int_{\tau=0}^1 c(p(\tau)) \left| \frac{d}{d\tau} p(\tau) \right| d\tau \right) \left| \frac{d}{dt} \xi_q(t) \right| dt. \quad (16)$$

We can derive the functional gradient with respect to a point p_i at time t_i , resulting in

$$\begin{aligned} \nabla J_{\text{occ}}(\xi_q, \xi_a, M)(t_i) = & \int_{\tau=0}^1 \nabla c(p(\tau)) |L| |\dot{q}| \left[I - \left(\hat{q} + \tau \left(\frac{\dot{a}}{|\dot{q}|} - \hat{q} \right) \right) \hat{q}^T \right] \\ & - c(p(\tau)) |\dot{q}| \left[\hat{L}^T + \frac{\hat{L}^T L \hat{q}^T}{|\dot{q}|} + |L| \kappa^T \right] d\tau, \end{aligned} \quad (17)$$

where

$$\begin{aligned} q &= \xi_q(t_i), \quad a = \xi_a(t_i), \quad p(\tau) = (1-\tau)q + \tau a, \quad L = a - q, \\ \hat{v} &= \frac{v}{\|v\|}, \quad \kappa = \frac{1}{\|\dot{q}\|^2} (I - \hat{q} \hat{q}^T) \ddot{q}. \end{aligned} \quad (18)$$

Intuitively, the term multiplying $\nabla c(p(\tau))$ is related to variations of the signed distance gradient in space, with the rest of the term acting as a lever to deform the trajectory. The term $c(p(\tau))$ is linked to changes in path length between camera and actor.

7.4 | Trajectory optimization algorithm

Our objective is to minimize the total cost function $J(\xi_q)$ (1). We do so by covariant gradient descent, using the gradient of the cost function $\nabla J(\xi_q)$, and an analytic approximation of the Hessian $\nabla^2 J(\xi_q) = (A_{\text{smooth}} + \lambda_3 A_{\text{shot}})$:

$$\xi_q^+ = \xi_q - \frac{1}{\eta} (A_{\text{smooth}} + \lambda_1 A_{\text{shot}})^{-1} \nabla J(\xi_q). \quad (19)$$

In the optimization context, $\nabla^2 J(\xi_q)$ acts as a metric to guide the solution towards the direction of the steepest descent of the functional cost. This step is repeated until convergence. We follow two conventional stopping criteria for descent algorithms based on current cost landscape curvature and relative cost decrease (Boyd & Vandenberghe, 2004), and limit the maximum number of iterations. We use the current trajectory as initialization for the next planning problem, appending a segment with the same curvature as the final points of the trajectory for the additional points until the end of the time horizon.

Note in Algorithm 2 one of the main advantages of the CHOMP algorithm (Ratliff, Zucker, et al., 2009): we only perform the Hessian matrix inversion once, outside of the main optimization loop, rendering good convergence rates (Bonatti et al., 2018). By fine-tuning hyper-parameters such as trajectory discretion level, trajectory time horizon length, optimization convergence thresholds, and relative weights between costs, we can achieve a replanning frequency of approximately 5 Hz considering a 10 s horizon. These are adequate parameters for safe and nonmyopic operations in our environments, but lower or higher frequencies can be achieved with the same underlying algorithm depending on application-specific requirements.

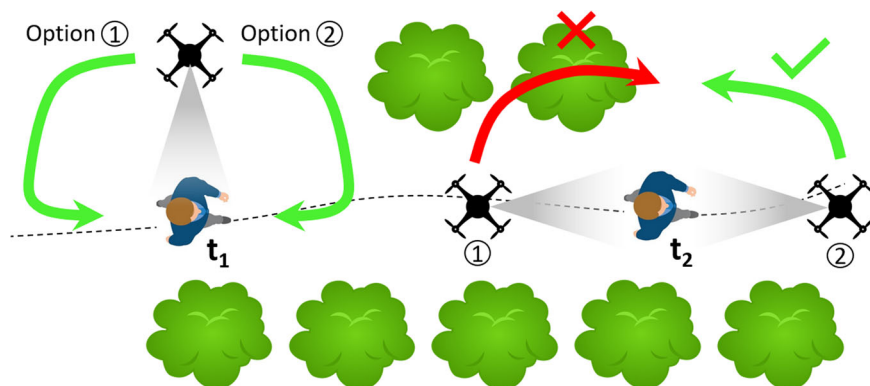
Algorithm 2: Optimize (ξ_q)

```

1  $M_{inv} \leftarrow (A_{smooth} + \lambda_3 A_{shot})^{-1};$ 
2 for  $i = 0, 1, \dots, i_{max}$  do
3   if  $(\nabla J(\xi_{qi})^T M_{inv} \nabla J(\xi_{qi}))^2 / 2 < \epsilon_0$  or  $(J(\xi_{qi}) - J(\xi_{qi-1})) < \epsilon_1$  then
4     return  $\xi_{qi};$ 
5   end
6    $\xi_{qi+1} = \xi_{qi} - \frac{1}{\eta} M_{inv} \nabla J(\xi_{qi});$ 
7 end
8 return  $\xi_{qi};$ 
```

The resulting trajectory from the most recent plan is appended to the UAV's trajectory tracker, which uses a PD controller to send velocity commands to the aircraft's internal controller.

FIGURE 15 Example of artistic parameter selection as a sequential decision-making problem. The choice of frontal or back shots at time step t_1 influence the quality of left side shot choice at time step t_2 [Color figure can be viewed at wileyonlinelibrary.com]



8 | LEARNING ARTISTIC SHOT SELECTION

In this section, we introduce a novel method for online artistic shot type selection. Parameter selection which specifies the shot type can be set before deployment with a fixed set of parameters Ω_{art} . However, using a fixed shot type renders undesirable results during operation since the UAV does not adapt to different configurations of obstacles in the environment. Instead, here we design an algorithm for selecting adaptive shot types, depending on the context of each scene.

8.1 | Deep reinforcement learning problem formulation

As introduced in Section 2, the choice of artistic parameters is a time-dependent sequential decision-making problem. Decisions taken at the current time step influence the quality of choices in future states. Figure 15 exemplifies the sequential nature of the problem.

We define the problem as a contextual Markov decision process (C-MDP; Krishnamurthy, Agarwal, & Langford, 2016), and use an RL algorithm to find an optimal shot selection policy. Our goal is to learn a policy $\pi_\theta(a_t|c_t)$, parametrized by θ , that allows an agent to choose an action a_t , given scene context c_t , to select among a discrete set of UAV artistic parameters Ω_{art} . Our action set is defined as four discrete values of Ω relative to left, right, back, and frontal shots. These shot types define the relative yaw angle ϕ_{rel} , which is fed into the UAV's motion planner, as explained in Section 7.

We define state c_t as the scene context, which is an observation drawn from the current MDP state s_t . The true state of the MDP is not directly observable because, to maintain the Markovian assumption, it encodes a diverse set of information such as: the UAV's full state and future trajectory, the actor's true state and future trajectory, the full history of shot types executed in past choices, a set of images that the UAV's camera has recorded so far, ground-truth obstacle map, environmental properties such as lighting and wind conditions, and so forth. Therefore, our definition of context c_t can be seen as a lower dimensional compression of s_t , given by a concatenation of the following three elements:

1. *Height map*: a local 2.5D map containing the elevation of the obstacles near the actor;
2. *Current shot type*: four discrete values corresponding to the current relative position of the UAV with respect to the actor;
3. *Current shot count*: number of time steps the current shot type has been executed consecutively.

We assume that states evolve according to the system dynamics: $s_{t+1} \sim p(s_t, a_t)$. Finally, we define the artistic reward $R_{\text{art}}(v_t)$ where $v_t(s_t, a_t) = \{l_1, l_2, \dots, l_k\}$ is the video taken after the UAV executed action a_t at state s_t . Our objective is to find the parameters of the optimal policy, which maximizes the expected cumulative reward:

$$\theta^* = \arg \max_{\theta} \mathbb{E} \left[\sum_{t=1}^T R_{\text{art}}(v_t) \right], \quad (20)$$

where the expectation accounts for all randomness in the model and the policy. A major challenge for solving Equation (20) is the difficulty of explicitly modeling the state transition function $p(s_t, a_t)$. This function is dependent on variables such as the quadrotor and actor dynamics, the obstacle set, the motion planner's implicit behavior, the quadrotor, and camera gimbal controllers, and the disturbances in the environment. In practice, we cannot derive an explicit model for the transition probabilities of the MDP. Therefore, we use a model-free method for the RL problem, using an action-value function $Q(c_t, a_t)$ to compute the artistic value of taking action a_t given the current context c_t :

$$Q(c_t, a_t) = \sum_{t'=t}^T \mathbb{E}_{\pi\theta}[R_{\text{art}}(v(c_t, a_t)) | c_t, a_t]. \quad (21)$$

The large size and complexity of the state space for our application motivates us to use a deep neural network with parameters θ to approximate Q : $Q(c_t, a_t) \approx f(c_t, a_t, \theta)$ (Mnih et al., 2013; Sutton & Barto, 1998).

8.2 | Reward definition

Now we define the artistic reward function R_{art} . At a high level, we define the following basic desired esthetical criteria for an incoming shot sequence:

- Keep the actor within camera view for as much time as possible;
- Maintain the tilt viewing angle θ_t within certain bounds; neither too low nor too high above the actor;
- Vary the relative yaw viewing angle over time, to show different sides of the actor and backgrounds. Constant changes keep the video clip interesting. However, too frequent changes do not leave the viewer enough time to get a good overview of the scene;
- Keep the drone safe, since collisions at a minimum destabilize the UAV and usually cause complete loss of actor visibility due to a crash.

While these basic criteria represent essential esthetical rules, they cannot account for all possible esthetical requirements. The evaluation of a movie clip can be highly subjective, and depend on the context of the scene and background of the evaluator. Therefore, in this study we compare two different approaches for obtaining numerical reward values. In the first approach, we hand-craft an arithmetical reward function R_{art} , which follows the basic esthetics requirements outlined above. In addition, we explore an alternative approach for obtaining R_{art} directly from human supervision. Next, we describe both methods.

8.2.1 | Hand-crafted reward

The reward calculation from each control time step involves the analysis and evaluation of each frame of the video clip. Since our system operates with steps that last 6 s, the reward value depends on the evaluation of 180 frames, given that images arrive at 30 Hz. We define R_{frame} as the subreward relative to each frame, and compute it using the following metrics:

Shot angle

$R_{\text{frame}}^{\text{shot}}$ considers the current UAV tilt angle θ_{rel} in comparison with an optimal value $\theta_{\text{opt}} = 15^\circ$ and an accepted tolerance $\theta_{\text{tol}} = \pm 10^\circ$ around it.² The shot angle subreward decays linearly and symmetrically between 1.0 and 0.0 from θ_{opt} to the tolerance bounds. Out of the bounds, we assign a negative penalty of $R_{\text{frame}}^{\text{shot}} = -0.5$.

Actor's presence ratio

Actor's presence ratio considers the screen space occupied by the actor's body. We set two bounds $pr_{\min} = 0.05$ and $pr_{\max} = 0.10$ based on a desired long-shot scale, actor size of 1.8 m, and the camera's intrinsic matrix. If the presence ratio lies within the bounds, we set the value of $R_{\text{frame}} = R_{\text{frame}}^{\text{shot}}$. Otherwise, this parameter indicates that the current frame contains a very low esthetics value, with the actor practically out of the screen or occupying an exorbitant proportion of it. In that case, we set a punishment $R_{\text{frame}} = -0.5$.

We average the resulting R_{frame} over all frames present in one control step to obtain an intermediate reward $R_{\text{step}} = \frac{1}{N} \sum_{i=1}^N R_{\text{frame}_i}$. Next, we consider the interaction between consecutive control steps to discount R_{step} using a third metric: shot type duration.

Shot type duration

It considers the duration of the current shot type, given by the count of steps c in which the same action was selected sequentially. We use the heuristic that the ideal shot type has a length 12 s, or $c_{\text{opt}} = 2$ time steps³, and define a variable discount parameter α_c , as seen in Figure 16. High repetition counts are penalized quadratically to maintain the viewers' interest in the video clip.

²The optimal value and bounds were determined by using standard shot parameters for aerial cinematography.

³This heuristics choice was based on informal tests with shot switching frequencies.

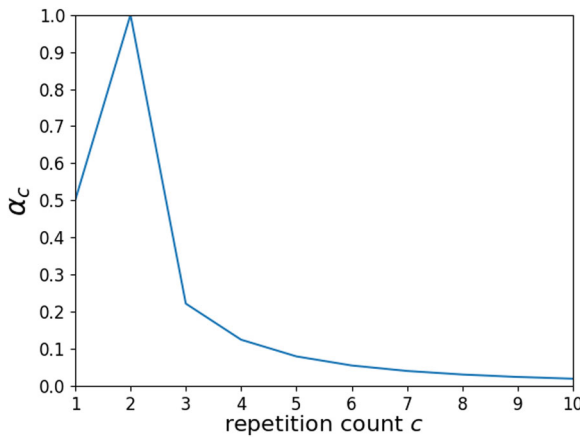


FIGURE 16 Values of the variable discount parameter α_c over shot repetition count c [Color figure can be viewed at wileyonlinelibrary.com]

Equation (22) shows how we obtain the final artistic reward R_{art} for the current movie clip. If R_{step} is positive, α_c serves as a discount factor, with the aim of guiding the learner towards the optimal shot repetition count. In the case of negative R_{step} , we multiply the reward by the inverse α_c , with the objective of accentuating the penalization and to incentivize the policy to quickly recover from executing bad shot types repetitively.

$$R_{\text{art}} = \begin{cases} R_{\text{step}} \cdot \alpha_c, & \text{if } R_{\text{step}} \geq 0, \\ \frac{R_{\text{step}}}{\alpha_c}, & \text{otherwise.} \end{cases} \quad (22)$$

In the eventual case of a UAV collision during the control step, we override the reward calculation procedure to only output a negative reward of $R_{\text{art}} = -1.0$.

Human supervision reward

We also explore a reward scheme for video segments based solely on human evaluation. We create an interface (Figure 17) in which the user gives an esthetics score between 1 (worst) and 5 (best) to the video generated by the previous shot selection action. The score is then linearly mapped to a reward R_{art} between -0.5 and 1.0 to update the shot selection policy in the RL algorithm. In the case of a crash during the control step, we override the user's feedback with a penalization of $R_{\text{art}} = -1.0$.

8.3 | Implementation details

Our deep Q-network (DQN) architecture is composed of different linear layers that combine the state inputs, as seen in Figure 18. We use ReLU functions after each layer except for the last, and use the Adam optimizer (Kingma & Ba, 2014) with Huber loss (Huber, 1964) for creating the gradients. We use an experience replay (ER) buffer for training the network, such as the one described by Mnih et al. (2015).

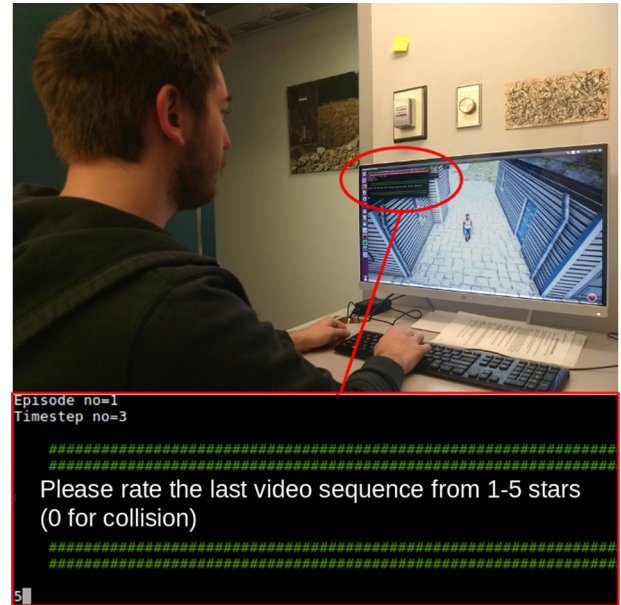


FIGURE 17 Evaluators rate video clips during the training procedure using an interface on the screen [Color figure can be viewed at wileyonlinelibrary.com]

9 | EXPERIMENTAL RESULTS

In this section, we detail integrated experimental results, followed by detailed results on each subsystem.

9.1 | Integrated system results

We conducted a series of field trials to evaluate our integrated system in real-life conditions. We used a large open facility named Gascola in Penn Hills, PA, located about 20 min east of Pittsburgh, PA. The facility has a diverse set of obstacle types and terrain types such as several off-road trails, large mounds of dirt, trees, and uneven terrain. Figure 19 depicts the test site and shows the different areas where the UAV flew during experiments. We summarize the test's objectives and results in Table 3, and indicate which results explain our initial hypotheses from Section 4.1.

Figure 20 summarizes our experiments conducted with fixed shot types. We employ a variety of shot types and actors, while operating in a wide range of unstructured environments such as open fields, in proximity to a large mound of dirt, on narrow trails between trees and on slopes. In addition, Figure 21 provides a detailed time-lapse of how the planner's trajectory output evolves during flight through a narrow trail between trees (Figure 22).

Figure 23 shows experiments where we employed the online automatic artistic selection module. The in-depth results of this module are described in Section 9.4.

We also summarize our integrated system's runtime performance statistics in Table 4, and discuss details of the online mapping performance in Figure 22. Videos of the system in action can be found attached to the submission, or online at <https://youtu.be/ookhHnqmlaU>.

From the field experiments, we verify that our system achieved all system-level objectives in terms of safely and robustly executing a

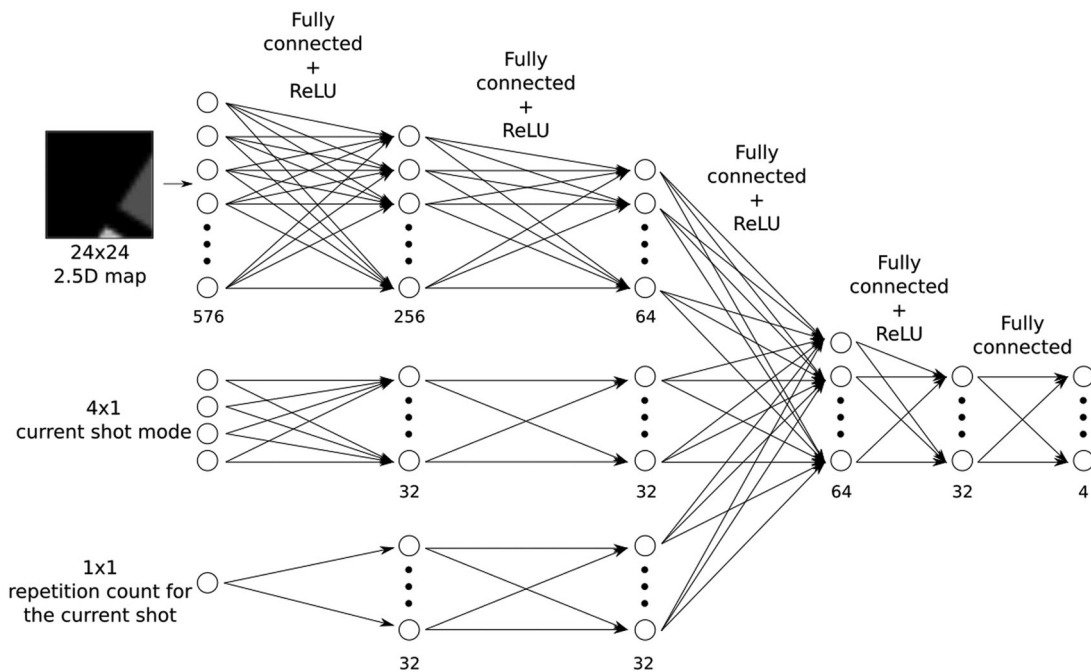


FIGURE 18 DQN architecture consisting of fully connected layers. Each portion of state is first fed to separate mini-networks of two layers. Then, the outputs of these are combined in three consecutive layers whose output is the Q values

diverse set of aerial shots with different actors and environments. Our data also confirms the questions raised to validate our hypotheses: onboard sensors and computing power sufficed to provide smooth plans, producing artistically appealing images.

Next we present detailed results on the individual subsystems of the aircraft.

9.2 | Visual actor localization and heading estimation

Here we detail data set collection, training, and testing of the different subcomponents of the vision module. We summarize the vision-specific test's objectives and results in Table 5.

9.2.1 | Object detection network

Data set collection

We trained the network on the COCO data set (Lin et al., 2014), and fine-tuned it with a custom aerial filming data set. To test, we manually labeled 120 images collected from our aerial filming experiments, with bounding box over people and cars.

Training procedure

We trained and compared two architectures: one based on Faster-RCNN, another on SSD. As mentioned in Section 5, we simplify feature extraction with MobileNet-based structure to improve efficiency. First, we train both structures on the COCO dataset. While the testing



FIGURE 19 Testing facility. The middle figure shows a top-down satellite view of testing terrain, overlaid with unmanned aerial vehicle positions from different trials. We accumulated over 2 hr of flight time and a total distance of almost 6 km. The side figures show the diverse types of terrains in our experiments. The figures also depict different actors and different seasons [Color figure can be viewed at wileyonlinelibrary.com]

TABLE 3 Objectives and results for integrated experiments

Objectives	Results
Stay safe among unstructured obstacles sensed online (addresses Hyp. 1)	Avoided all obstacles successfully, including trees, dirt mound, slopes, posts. See Figures 20–21.
Avoid occlusions among any obstacle shape (addresses Hyp. 1)	Planner maintained actor visibility. See Figure 20. More results in Section 9.3.
Process data fully onboard (addresses Hyp. 1)	Data processed solely on onboard computer. Table 4 and Figure 22 show system statistics.
Operate with different types of actors at different speeds (addresses Hyps. 2 and 3)	Person, car, bikes shot at high-speed chases. See Figures 20–23.
Execute different shot types (addresses Hyp. 3)	Successful recording of back, right, front, circling shots (Figure 20). Smooth shot transitions (Figure 23).
Automatically select artistically meaningful shot types (addresses Hyp. 3)	Policy adapted to current context to produce a visually esthetic video (Figure 23).

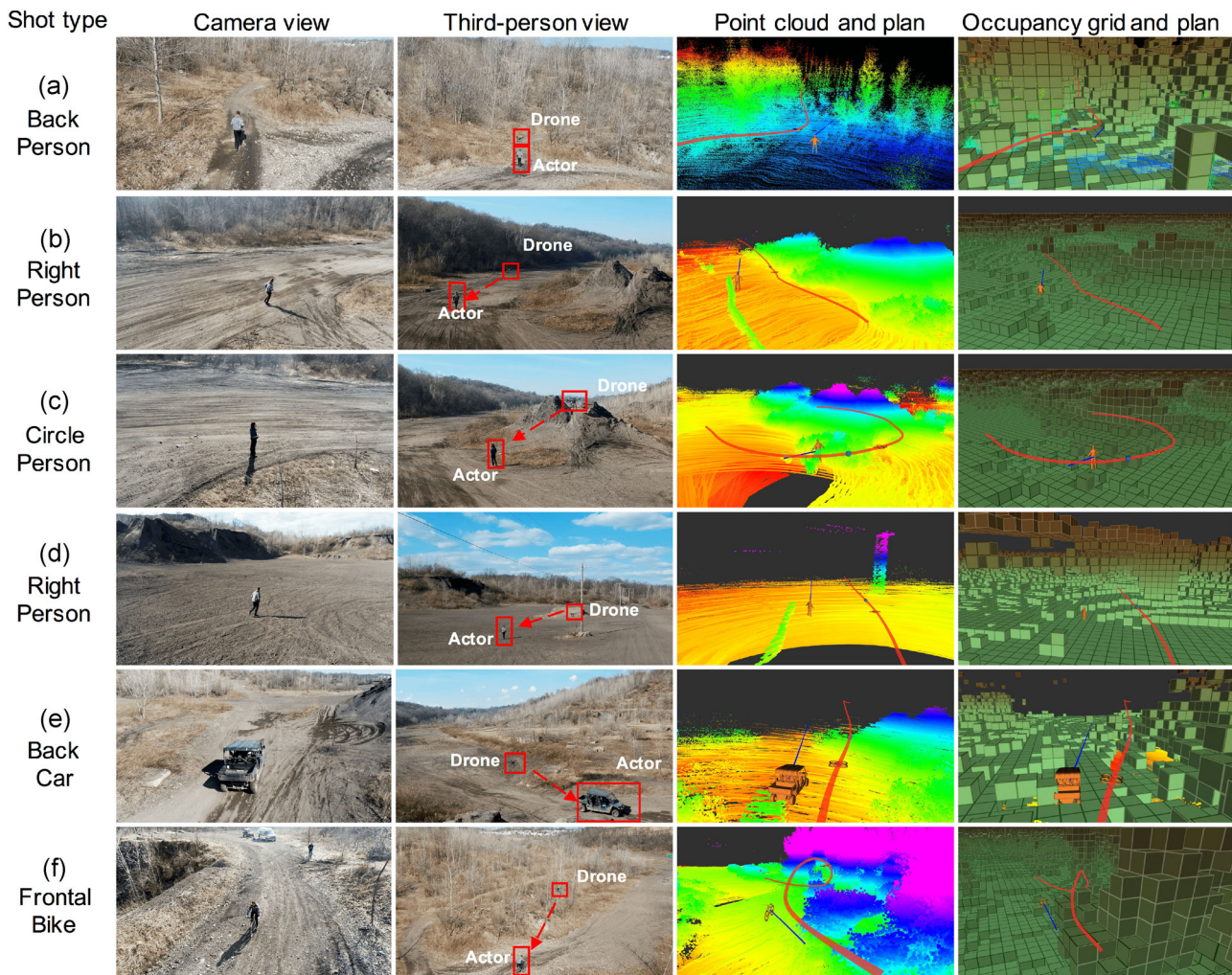


FIGURE 20 Field results with different fixed shot types in multiple environment types, following different actor types. The UAV trajectory (red) tracks the actor's forecasted motion (blue) and stays safe while avoiding occlusions from obstacles. We display accumulated point clouds of LiDAR hits and the occupancy grid: (a) Back shot following runner in narrow tree trail; (b) Right-side shot following a runner close to dirt mound; (c) Circular shot on person close to dirt mound; (d) Right-side shot below the 3D structure of an electric wire. Note that LiDAR registration is noisy close to the pole in a row due to large electromagnetic interference with the UAV's compass; (e) Right-side shot following car close to dirt mound; (f) Frontal shot on biker going downhill on a trail with tall trees. UAV, unmanned aerial vehicle [Color figure can be viewed at wileyonlinelibrary.com]

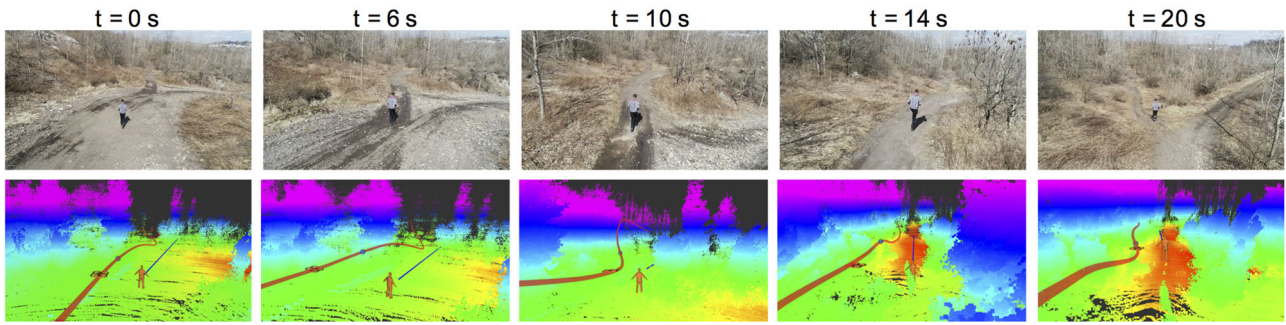


FIGURE 21 Detailed time-lapse of back shot following a runner in a narrow trail with trees. As the unmanned aerial vehicle approaches the trees at $t = 6$ s, the trajectory bends to keep the vehicle safe, maintain target visibility, and follow the terrain's downward inclination [Color figure can be viewed at wileyonlinelibrary.com]

performance is good on the COCO testing data set, the performance shows a significant drop, when tested on our aerial filming data. The network has a low recall rate (lower than 33%) due to the big angle of view, distant target, and motion blur. To address the generalization problem, we augmented the training data by adding blur, resizing and cropping images, and modifying colors. After training on a mixture of COCO data set (Lin et al., 2014) and our own custom data set as described in Section 5, Figure 24 shows the recall-precision curve of

the two networks when tested on our filming testing data. The SSD-based network has difficulties detecting small objects, an important need for aerial filming. Therefore, we use Faster-RCNN-based network in our experiments and set the detection threshold to precision = 0.9, as shown with the green arrow in Figure 24.

9.2.2 | HDE network

Data set collection

We collected a large number of image sequences from various sources. For the person HDE, we used two surveillance data sets: VIRAT (Oh et al., 2011) and DukeMCMT (Ristani et al., 2016), and one action classification data set: UCF101 (Soomro, Zamir, & Shah, 2012). We manually labeled 453 images in the UCF101 data set as ground-truth HDE. As for the surveillance data sets, we adopted a semiautomatic labeling approach where we first detected the actor in every frame, then computed the ground-truth heading direction based on the derivative of the subject's position over a sequence of consecutive time frames. For the car HDE we used two surveillance data sets, VIRAT, and Ko-PER (Strigel, Meissner, Seeliger, Wilking, & Dietmayer, 2014), in addition to one driving data set, PKU-POSS (C. Wang et al., 2016). Table 6 summarizes our data.

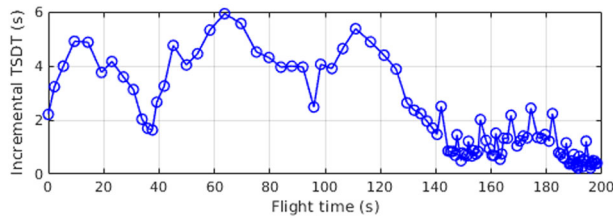


FIGURE 22 Incremental distance transform computation time over flight time. The first operations take significantly more time because of our map initialization scheme where all cells are initially considered as unknown instead of free, causing the first laser scans to update a significantly larger number of voxels than later scans. During calculation the planner is not blocked: it can still access TS DT values from the latest version of M . TS DT, truncated signed distance transform [Color figure can be viewed at wileyonlinelibrary.com]

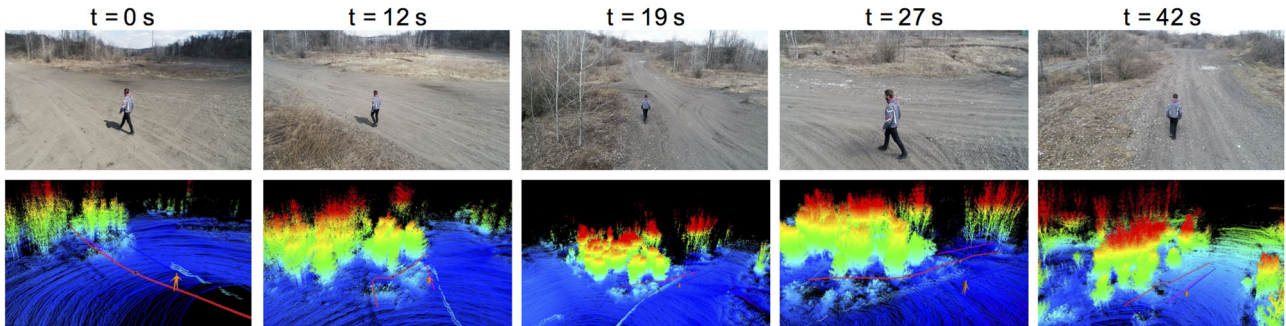


FIGURE 23 Field test results using the online artistic shot selection module. UAV trajectory is shown in red, actor motion forecast in blue, and desired shot reference in pink. The UAV initially does a left side shot at $t = 0$ s in the open field, but as a line of trees appear, it switches to a back shot at $t = 12$ s. When an opening appears among the tree lines, the UAV selects a left-side shot again at $t = 27$ s, and when the clearance ends, the module selects a back shot again. UAV, unmanned aerial vehicle [Color figure can be viewed at wileyonlinelibrary.com]

TABLE 4 System statistics recorded during flight time on the onboard computer

System	Module	CPU			Target freq. (Hz)
		Thread (%)	RAM (MB)	Runtime (ms)	
Vision	Detection	57	2,160	145	15
	Tracking	24	25	14.4	
	Heading	24	1,768	13.9	
	KF	8	80	0.207	
Mapping	Grid	22	48	36.8	
	TSDF	91	810	100–6,000	10
	LiDAR	24	9	100	
Planning	Planner	98	789	198	5
Controls	DJI SDK	89	40	NA	50
Shot selection	DQN	4	1,371	10.0	0.16

Training the network

We first train the HDE network using only labeled data from the data sets shown in Table 6. Rows 1–3 of Table 7 display the results. Then, we fine-tune the model with unlabeled data to improve generalization.

We collected 50 videos, each contains approximately 500 sequential images. For each video, we manually labeled six images. The HDE model is finetuned with both labeled loss and continuity loss, same as the training process on the open accessible data sets. We qualitatively and quantitatively show the results of HDE using semisupervised finetuning in Figure 25 and Table 7. The experiment verifies our model could generalize well to our drone filming task, with an average angle error of 0.359 rad. Compared to pure supervised learning, utilizing unlabeled data improves generalization and results in more robust and stable performance.

Baseline comparisons

We compare our HDE approach against two baselines. The first baseline Vanilla-CNN is a simple CNN inspired by Choi, Lee, and Zhang (2016). The second baseline CNN-GRU implicitly learns temporal continuity using a GRU network inspired by P. Liu, Liu, and Ma (2017). One drawback for this model is that although it models the temporal continuity implicitly, it needs large number of labeled sequential data for training, which is very expensive to obtain.

TABLE 5 Objectives and results for vision-specific experiments

Objectives	Results
Compare object detection network architectures	Faster-RCNN showed significantly better performance than SSD architecture (Figure 24).
Compare supervised and semisupervised methods for heading estimation	Semisupervised method has smoother output and higher accuracy (Table 7 and Figure 25).
Analyze the amount of labeled data needed for semisupervised training	Loss increased by less than ~8% when we trained the model with 1/10 of labeled data (Figure 26).
Validate integrated 3D pose estimator using image projections	Error of less than 1.7 m in estimated actor path length over a 40 m long ground-truth actor trajectory (Figure 27).

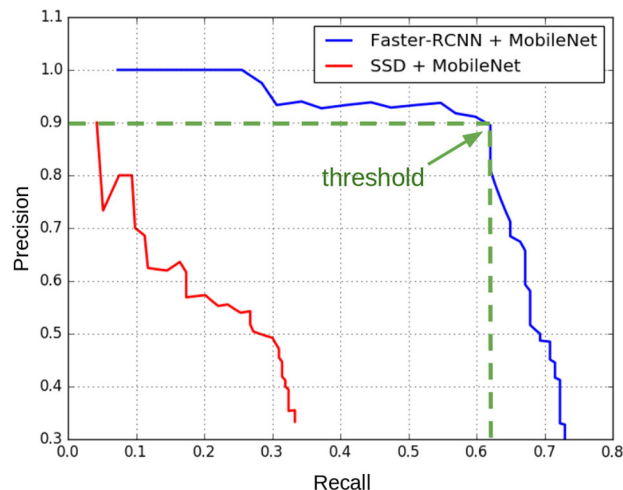


FIGURE 24 Precision recall curve for object detection. The results are tested on the filming testing data, which contains many challenging cases. R-CNN, R-convolutional neural network; SSD, single-shot detector [Color figure can be viewed at wileyonlinelibrary.com]

We employ three metrics for quantitative evaluation: (a) Mean square error (MSE) between the output ($\cos\theta, \sin\theta$) and the ground truth ($\hat{\cos}\theta, \hat{\sin}\theta$). (b) Angular difference (AngleDiff) between the output and the ground truth. (c) Accuracy obtained by counting the percentage of correct outputs, which satisfies $\text{AngleDiff} < \pi/8$. We use the third metric, which allows small error, to alleviate the ambiguity in labeling human heading direction.

Vanilla-CNN (Choi et al., 2016) and CNN-GRU (P. Liu et al., 2017) baselines trained on open datasets do not transfer well to drone filming data set with accuracy below 30%. Our SSL-based model trained on open data sets achieves 48.7% accuracy. By finetuning on labeled samples of drone filming, we improve this to 68.1%. Best performance is achieved by finetuning on labeled and unlabeled sequences of the drone filming data with accuracy of 72.2% (Table 7).

Reduction in required labeled data using SSL

Following Section 5, we show how SSL can significantly decrease the number of labeled data required for the HDE task.

In this experiment, we train the HDE network on the DukeMCMT data set, which consists of 274 k labeled images from eight different surveillance cameras. We use the data from seven cameras for

TABLE 6 Data sets used in heading direction estimation study

Data set	Target	GT	No. of Seqs	No. of Imgs
VIRAT	Car/person	MT*	650	69,680
UCF101	Person	HL(453)*	940	1,18,027
DukeMCMT	Person	MT*	4,336	2,74,313
Ko-PER	Car	✓	12	18,277
PKU-POSS	Car	✓	-	28,973

training, and one for testing (about 50 k). Figure 26 compares the result from the proposed semisupervised method with a supervised method using a different number of labeled data. We verify that by utilizing unsupervised loss, the model generalizes better to the validation data than the one with purely supervised loss.

As mentioned, in practice, we only use 50 unlabeled image sequences, each containing approximately 500 sequential images, and manually labeled 300 of those images. We achieve comparable performance with purely supervised learning methods, which require more labeled data.

9.2.3 | 3D pose estimation

Based on the detected bounding box and the actor's heading direction in 2D image space, we use a ray-casting method to calculate the 3D pose of the actor, given the online occupancy map and the camera pose. We assume the actor is in an upward pose, in which case the pose is simplified as (x, y, z, ψ_a^w) , which represents the position and orientation in the world frame.

We validate the precision of our 3D pose estimation in two field experiments where the drone hovers and visually tracks the actor. First, the actor walks between two points along a straight line, and we compare the estimated and ground-truth path lengths. Second, the actor walks in a circle at the center of a football field, and we compute the errors in estimated position and heading direction. Figure 27 shows our estimation error is less than 5.7%.

TABLE 7 Semisupervised fine tuning results

Method	MSE loss	AngleDiff (rad)	Accuracy (%)
Vanilla-CNN w/o finetune	0.53	1.12	26.67
CNN-GRU w/o finetune	0.5	1.05	29.33
SSL w/o finetune	0.245	0.649	48.7
SL w/finetune	0.146	0.370	68.1
SSL w/finetune	0.113	0.359	72.2

Abbreviations: CNN, convolutional neural network; MSE, mean square error; SL, supervised learning; SSL, semisupervised learning.

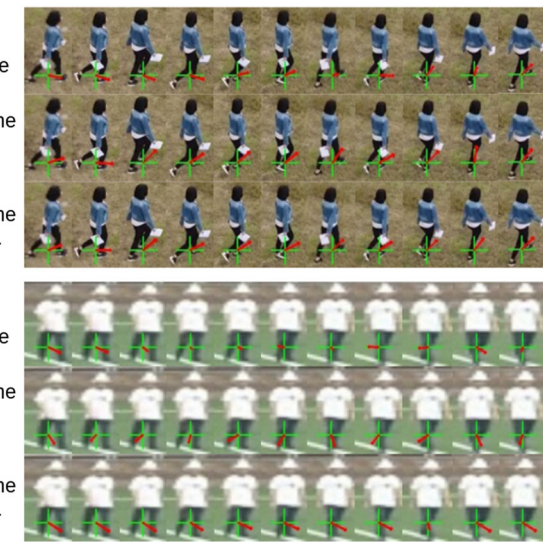


FIGURE 25 Three models are tested on the sequential data. Two testing sequences are shown in this figure. The top row of each testing sequence shows the results that directly employ the model trained on other open accessible data sets to the aerial filming task. It generalizes poorly due to the distribution difference. The middle row and bottom row show the results after finetuning the model on the filming data with and without continuity loss, respectively. The model using continuity loss for finetuning (bottom row) outputs more accurate and smooth results. SL, supervised learning; SSL, semisupervised learning [Color figure can be viewed at wileyonlinelibrary.com]

9.3 | Planner evaluation

Next we present detailed results on different aspects of the UAV's motion planner. Table 8 summarizes the experiments' objectives and results.

9.3.1 | Ground-truth obstacle map versus online map

We compare average planning costs between results from a real-life test where the planner operated while mapping the environment in real-time with planning results with the same actor trajectory but with full knowledge of the map beforehand. Results are averaged over 140 s of flight and approximately 700 planning problems. Table 9 shows a small increase in average planning costs with an online map, and Figure 28 shows that qualitatively both trajectories differ minimally. The planning time, however, doubles in the online mapping case due to mainly two factors: extra load on CPU from other system modules, and delays introduced by accessing the map that is constantly being updated. Nevertheless, computation time is low enough such that the planning module can still operate at the target frequency of 5 Hz.

Ground-truth actor pose versus the noisy estimate

We compare the performance between simulated flights where the planner has full knowledge of the actor's position versus artificially noisy estimates with 1 m amplitude of random noise. The qualitative

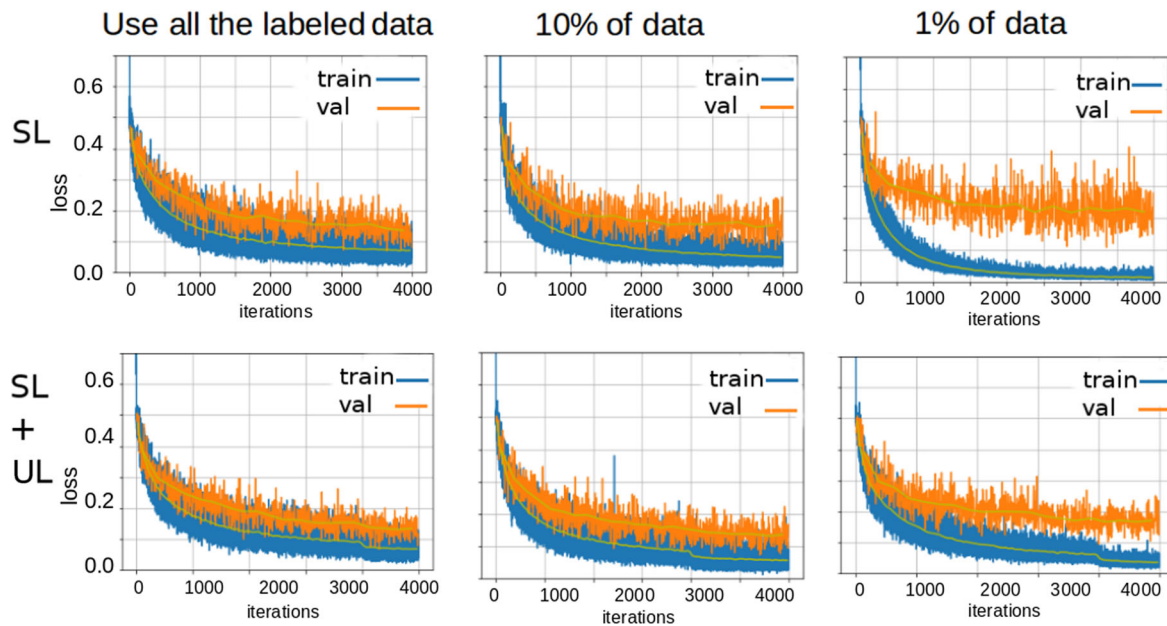


FIGURE 26 The top row shows training and validation loss for supervised learning using different number of labeled data. The validation performance drops from 0.13 to 0.22, when decreasing the number of labeled data from 100% to 1%. The bottom row shows results with semisupervised learning. The validation losses are 0.13, 0.14, and 0.17 respectively for 100%, 10%, and 1% labeled data [Color figure can be viewed at [wileyonlinelibrary.com](#)]

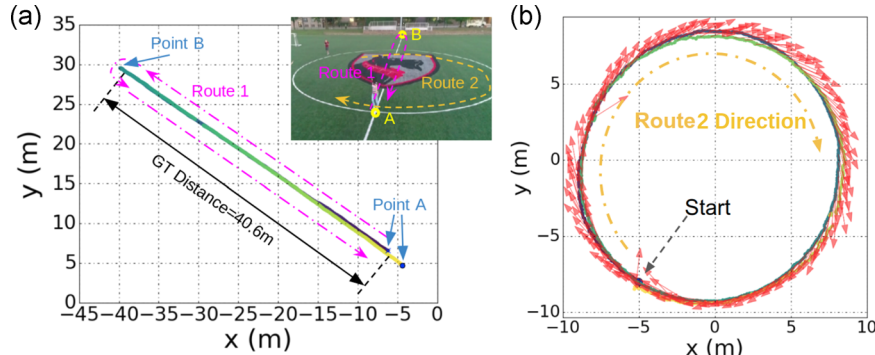


FIGURE 27 Pose and heading estimation results. (a) Actor walks on a straight line from points A-B-A. Ground-truth trajectory length is 40.6 m, while the estimated motion length is 42.3 m. (b) The actor walks along a circle. Ground-truth diameter is 18.3 m, while the estimated diameter from ray-casting is 18.7 m. Heading estimation appears tangential to the ground circle [Color figure can be viewed at [wileyonlinelibrary.com](#)]

TABLE 8 Objectives and results for detailed motion planner experiments

Objectives	Results
Performance comparison between online vs. ground-truth map	Similar path quality, with increase in planning time. See Figure 28 and Table 9.
Performance comparison between noisy actor forecast vs. ground-truth actor positioning	Similar path quality: smoothness cost handles noisy inputs. See Figure 29.
Confirm ability to operate in full 3D environments	Can fly under 3D obstacles, not only height maps. See Figure 20d.
Performance comparison between different planning time horizons	Longer horizons significantly improve path quality. See Figure 30 and Table 10.
Test impact of occlusion cost function on actor visibility	Occlusion cost significantly improves path quality. See Figures 32 and 31, and Table 11.

TABLE 9 Performance comparison between ground-truth and online map

Planning condition	Avg. plan time (ms)	Avg. cost	Median cost
Ground-truth map	32.1	0.1022	0.0603
Online map	69.0	0.1102	0.0825

comparison with the actor's ground-truth trajectory shows close proximity of both final trajectories, as seen in Figure 29.

Operation on unstructured 3D map

As seen in Figure 20d, our current system is able to map and avoid unstructured obstacles in 3D environments such as wires and poles. This capability is a significant improvement over previous work that only deals with ellipsoidal obstacle representations (Huang, Gao, et al., 2018; Joubert et al., 2016; Nägeli et al., 2017), or a height map assumption (Bonatti et al., 2018).

Advantage of longer planning horizons

We evaluate the overall system behavior when using different planning time horizons between 1 and 20 s, as seen in Table 10. Short horizons reason myopically about the environment, and cannot render robust and safe behavior in complex scenes, thus increasing the normalized cost per time length of the resulting trajectory. Figure 30 displays the qualitative difference between trajectories, keeping all variables except planning horizon constant.

Qualitative role of the occlusion cost function

For this experiment, unlike the tests with visual actor localization, we detect the actor using a ground-truth GPS tag. We set up the motion planner to calculate the UAV paths with and without the occlusion cost function, keeping all other scenario variables equal. As seen in Figure 31, our proposed occlusion cost significantly improves the esthetics of the resulting image, keeping the actor visibility. In addition to esthetics, maintaining actor visibility is a vital feature of our architecture, allowing vision-based actor localization.

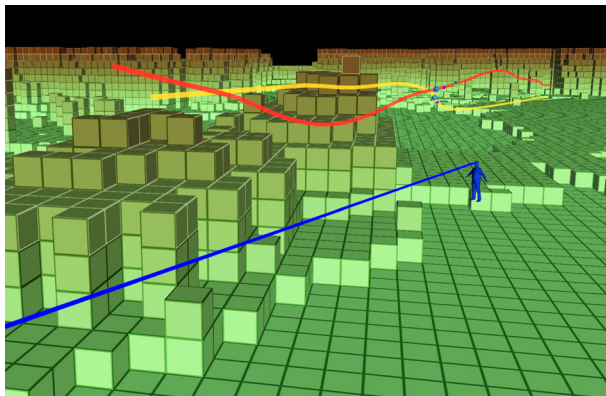


FIGURE 28 Performance comparisons between planning with full knowledge of the map (yellow) vs. with online mapping (red), displayed over the ground truth map grid. Online map trajectory is less smooth due to imperfect LiDAR registration and new obstacle discoveries as the flight progresses [Color figure can be viewed at wileyonlinelibrary.com]

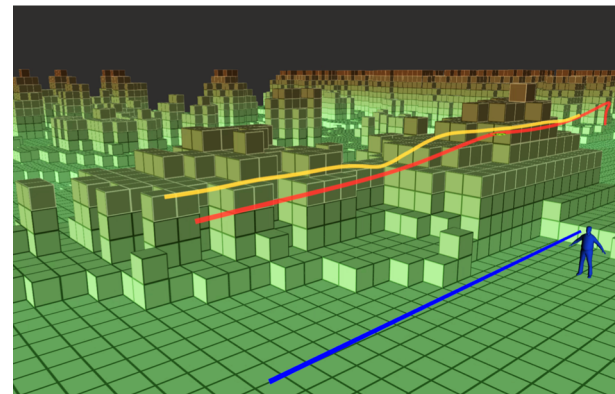


FIGURE 29 Performance comparison between planning with the perfect ground truth of the actor's location (red) vs. noisy actor estimate with artificial noise of 1 m amplitude (yellow). The planner is able to handle noisy actor localization well due to smoothness cost terms, with a final trajectory similar to the ground-truth case [Color figure can be viewed at wileyonlinelibrary.com]

The quantitative role of the occlusion cost function

We evaluate our planning algorithm on environments with increasing levels of randomized clutter, as seen in Figure 32. Table 11 summarizes the planner performance in different environments in terms of actor visibility and the average distance to the artistically desired trajectory. By using the occlusion cost function, we improve actor visibility by over 10% in comparison with pure obstacle avoidance in environments with 40 random spheres; however, the trade-off is an increase in the average distance to the desired artistic trajectory.

These detailed results allow us to draw insights into the planner performance under different conditions: it can operate smoothly, in full 3D maps, even under the noise of real-time environment mapping and noisy actor inputs. We can also verify the importance of the efficient optimization algorithm for planning: by allowing longer time horizons, we can generate significantly higher quality plans. Finally, we demonstrate the essential role of our occlusion cost, which is defined for arbitrary obstacle shapes in the environment, in maintaining actor visibility.

9.4 | Artistic shot selection

Next, we present detailed results on training and testing the artistic shot selection module, as well as experiments that provide insights to understand which artistic concepts this subsystem is learning. Table 12 summarizes our test objectives and results.

TABLE 10 Performance of motion planner with varying planning time horizons for the environment shown in Figure 30

Planning horizon length [s]	1.0	5.0	10.0	20.0
Normalized trajectory cost (J/t_f)	0.0334	0.0041	0.0028	0.0016
Computing time (ms)	0.0117	0.0131	0.0214	0.0343

Note: Longer planning horizons allow better reasoning for safety and occlusion avoidance, lowering the normalized planning cost. However, longer horizons naturally increase planning computing time.

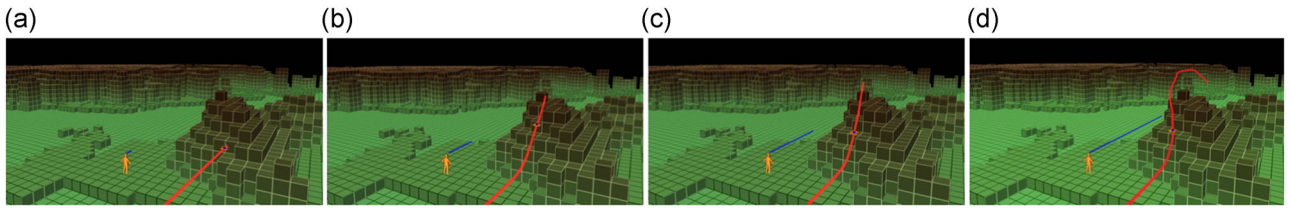


FIGURE 30 Planner behavior with different time horizons of 1 (a), 5 (b), 10 (c), and 20 (d) seconds for the same actor trajectory and environment. The shortest time horizon of 1 s is not sufficient for the planner to find a trajectory that avoids the mound, and the vehicle gets stuck in a bad local minimum of solutions. Longer horizons let the UAV plan more intelligent trajectories, reasoning about obstacle shapes long before the UAV reaches those positions. UAV, unmanned aerial vehicle [Color figure can be viewed at [wileyonlinelibrary.com](#)]

We trained our agent exclusively in simulation, using the Microsoft AirSim release (see Section 4.4). We organize our environments in three categories:

- **BlockWorld:** It is generated from a height map, and the actor walks on a path with alternating blocks on the left and right sides. Blocks have varying heights and lengths (Figure 33a).
- **BigMap:** It is generated from a height map, and significantly more complex. It is separated into three zones: one that resembles the BlockWorld environment, a second zone with alternating pillars, and a third zone with different shapes of mound-like structures (Figure 33b).

- **Neighborhood:** Unlike the two previous height maps, this environment is a photo-realistic rendering of a suburban residential area. The actor walks among structures like streets, houses, bushes, trees, and cars (Figure 33c).

9.4.1 | Learning an artistic policy

Hand-crafted reward

Using the hand-crafted reward definition from Section 8, we train a total of six policies in different environments. For all policies except

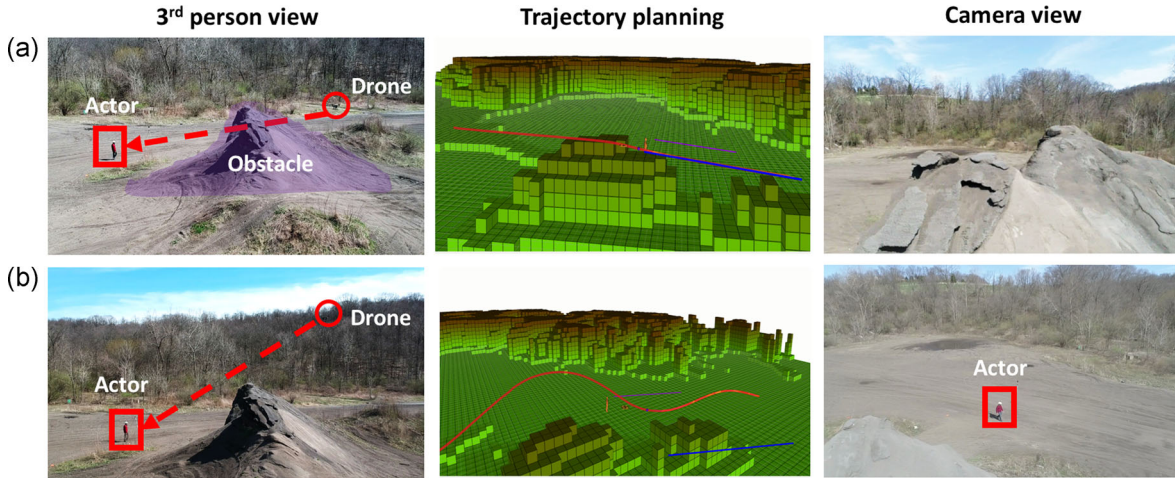


FIGURE 31 Comparison of planning (a) without and (b) with occlusion cost function in a special setup where actor positioning comes from a GPS tag. The occlusion cost function significantly improves the quality of the camera image in comparison with pure obstacle avoidance, for same shot type [Color figure can be viewed at [wileyonlinelibrary.com](#)]

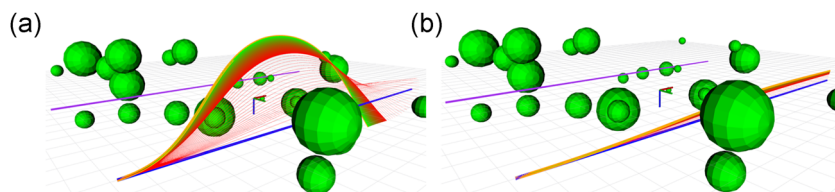


FIGURE 32 A randomized environment with obstacles to evaluate planner robustness. Unmanned aerial vehicle trajectory initialization shown in blue, actor trajectory in purple, and planner iterations vary from red to green (final solution). (a) Solution including occlusion cost function and (b) pure obstacle avoidance [Color figure can be viewed at [wileyonlinelibrary.com](#)]

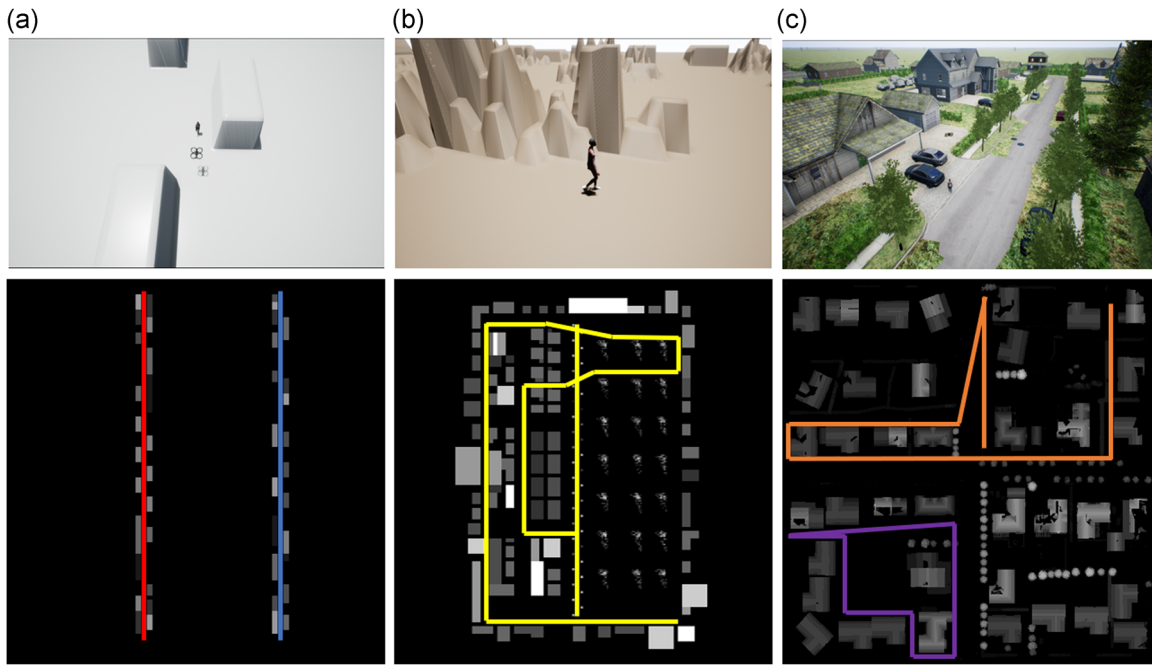


FIGURE 33 Rendering and height maps of AirSim environments with training routes. (a) BlockWorld 1 (red) and BlockWorld 2 (blue); (b) Bigmap (yellow); (c) Neighborhood 1 (orange) and Neighborhood 2 (purple) [Color figure can be viewed at wileyonlinelibrary.com]

Neighborhood 1 roam, the actor walks along a predefined path. We define each episode as a concatenation of five consecutive time steps, each with a duration of 6 s, and we train each policy between 300 and 2,000 episodes, depending on the complexity of the environment:

- *BlockWorld 1 and 2*: Trained in different randomized BlockWorld environments, BW1 and BW2, for 300 episodes.
- *BigMap*: Trained in a randomized BigMap environment, BM, for 1,500 episodes.
- *Neighborhood 1 and 2*: Trained in different sections of the Neighborhood environment, NH1 and NH2. Trained for 500 episodes.
- *Neighborhood roam*: Trained in the entirety of the Neighborhood environment NH, with actor walking in random motion, for 2,000 episodes.

We test all policies in all environments to evaluate generalizability. Table 13 summarizes the quantitative results. As expected, all policies perform better than random choice, and we achieve highest testing

rewards in the same environments the policies were trained in. We also verify that the best generalization performance occurs when policies are trained and tested on the same environment category. It is interesting to note that policies trained on the neighborhood environments tested on BigMap perform significantly better than those trained on BlockWorld, likely due to the simple geometry of the BlockWorld obstacles.

Figures 34 and 36 show examples of trajectories generated with trained policies. In addition, Figure 35 shows a heatmap with different actions, providing insights into the learned policy's behavior. Qualitatively, we observe that the learned behavior matches the intended goals:

- Keeps the actor in view by avoiding drastic shot mode switches between opposite positions such as left and right or front and back, which often cause visual loss of the actor;
- Switches shot types regularly to keep the viewer's interest;
- Avoids flying above high obstacles to keep the shot angle within desirable limits;
- Avoids high obstacles to maintain aircraft safety.

Human-generated rewards

Using the interface described in Section 8, we use human esthetics evaluations as rewards to train two new policies in the BlockWorld and Neighborhood environments for 300 and 500 episodes, respectively. Comparisons between both reward schemes are presented next.

9.4.2 | User study results

We asked 10 participants to watch 30 s video clips taken from four different policies in five different scenes. Each participant

TABLE 11 Evaluation of motion planner performance in the randomized environment from Figure 32

Success metric	Cost functions	No. of spheres in environment		
		1	20	40
Actor visibility along trajectory (%)	$J_{\text{occ}} + J_{\text{obs}}$	99.4 ± 2.2	94.2 ± 7.3	86.9 ± 9.3
	J_{obs}	98.8 ± 3.0	87.1 ± 8.5	75.3 ± 11.8
Avg. dist. to ξ_{shot} (m)	$J_{\text{occ}} + J_{\text{obs}}$	0.4 ± 0.4	6.2 ± 11.2	10.7 ± 13.2
	J_{obs}	0.05 ± 0.1	0.3 ± 0.2	0.5 ± 0.3

Note: Statistics computed using 100 random configurations for each environment complexity level.

TABLE 12 Objectives and results for artistic shot selection

Objectives	Results
Compare policy generalizability to different environments	Learned policies generalized well to new unseen environments. Table 13 compares performances.
Analyze role of specific environment context in policy behavior	Policy learned to actively avoid potential occlusions and switch often to keep video interesting (Figures 34–35).
Evaluate policies against baselines using real human esthetics in user study	Our policy outperformed constant shot types or random actions (Table 14 and Figure 36).
Transfer policy learned in simulation to real-life environments	We deployed the policy in additional field experiments (Figure 37).

ranked clips from most to least visually pleasing, and wrote open-ended comments on each clip. We chose two scenes from the BlockWorld and three from the Neighborhood environments, and compared the highest-performing hand-crafted reward policy for each environment against the human-generated reward policy. In addition, we included a constant back shot policy and a random action policy for comparison.

Table 14 summarizes the user study results, and Figure 36 shows the best-rated drone trajectories for each scene. As seen in Table 14, the trained policies using both reward schemes have higher ratings in all scenes than the random or constant back shot policies.

On average, the hand-crafted rewards produced policies were ranked better than those trained with human-defined rewards, although participants' opinions were the opposite in a few cases. We also summarize the participant's comments on the clips:

- All participants criticize the back shot policy as "boring" or "unexciting";
- All participants mentioned that the random policy loses view of the actor too often;
- The most common esthetics complaint is due to the loss of actor visibility;
- Participants often complained about too little camera movement when only one shot type is used for the entire 30 s clip. They also complained about camera movements being visually unpleasing when the shot type changes at every time step (every 6 s);

TABLE 13 Average reward per time step

Policy test env.	BW1	BW2	BM	NH1	NH2
BlockWorld 1	0.3444	<u>0.3581</u>	0.3635	0.3622	0.2985
BlockWorld 2	<u>0.3316</u>	0.3718	0.3918	0.4147	0.3673
BigMap	0.2178	0.2506	0.5052	0.5142	0.5760
Neighborhood 1	0.1822	0.1916	0.4311	0.5398	<u>0.5882</u>
Neighborhood 2	0.0813	0.1228	<u>0.4488</u>	0.4988	0.5897
Neighborhood 1 roam	0.1748	0.1779	0.4394	<u>0.5221</u>	0.5546
Random choice	-0.0061	0.0616	0.1944	0.2417	0.2047

Note: As expected, policies have the highest rewards when trained and tested on the same environment (bold diagonal). The second-best policy for each environment is underlined and italicized.

- Participants frequently mention that they like to see an overview of the surrounding environment and not only viewpoints with no scene context where the actor's background is just a building or wall. Clips, where the UAV provides multiple viewpoints, were positively marked;
- The human reward policy was often described as the most exciting one, while the hand-crafted reward policy was described as very smooth.

The main perceived difference between the hand-crafted reward policy and the human reward policy was the consistency of switching shots. While the former tries to switch shots every two time steps (12 s) if not disturbed by an obstacle, the latter is more irregular in timing. From the user studies, it is evident that a more regular period that is neither too short nor too long improves esthetic scores.

9.4.3 | Extended results in field experiments

We tested our trained policies in real-life settings. Since these tests were only focused on the shot selection module we operated using a

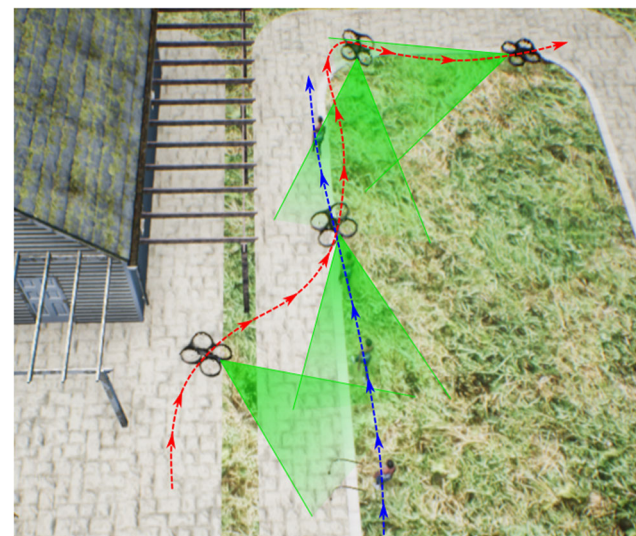


FIGURE 34 Time-lapse of drone trajectory during filming in a photo-realistic environment. Since the left-hand side is occupied, the drone switches from left to front and then right shot [Color figure can be viewed at wileyonlinelibrary.com]

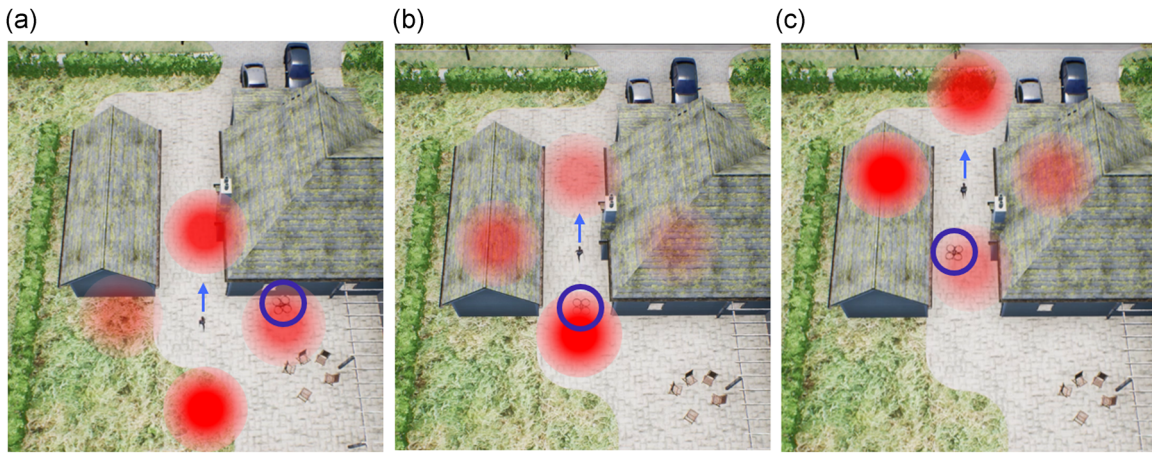


FIGURE 35 Visualization of the Q values of the DQN during testing corresponding to the four shot types. The more opaque a circle is, the higher is the action's Q value. The drone position before each decision is indicated by a blue ring around the drone. The drone starts on the right side of the actor and switches to back shot mode to traverse a narrow passage (a) where it stays in the actor's back for one-time step (b). Finally, it decides to switch to a left-side shot once the obstacles are passed (c) [Color figure can be viewed at [wileyonlinelibrary.com](#)]

premapped environment, differently than the integrated results from Section 9.1 that uses online mapping. We filmed scenes using three distinct policies: one trained with hand-crafted rewards on the *BigMap* environment, a second fixed back shot policy and a third random policy. Figure 37 summarizes the results.

Similar to the simulation results, the random policy results in constant loss of actor due to drastic position changes and

close proximity to obstacles. For example, a random action of the right shot will cause the UAV to climb much above the actor if it is too close to a large mound. The back shot policy, although stable in vehicle behavior, results in visually unappealing movies. Finally, our trained policy provides a middle ground, resulting in periodic changes in the UAV viewpoint, while providing stable visual tracking.

TABLE 14 Average normalized user-study score of video clips between 0 (worst) and 10 (best)

	Average	Scene 1	Scene 2	Scene 3	Scene 4	Scene 5
Hand-crafted reward	8.2	10.0	5.3	9.3	7.7	8.7
Human reward	7.1	5.0	9.0	6.0	7.7	8.0
Back shot	3.8	4.0	4.7	4.3	4.0	2.0
Random	0.9	1.0	1.0	0.3	0.7	1.3

Note: The best score for each scene is highlighted in bold.

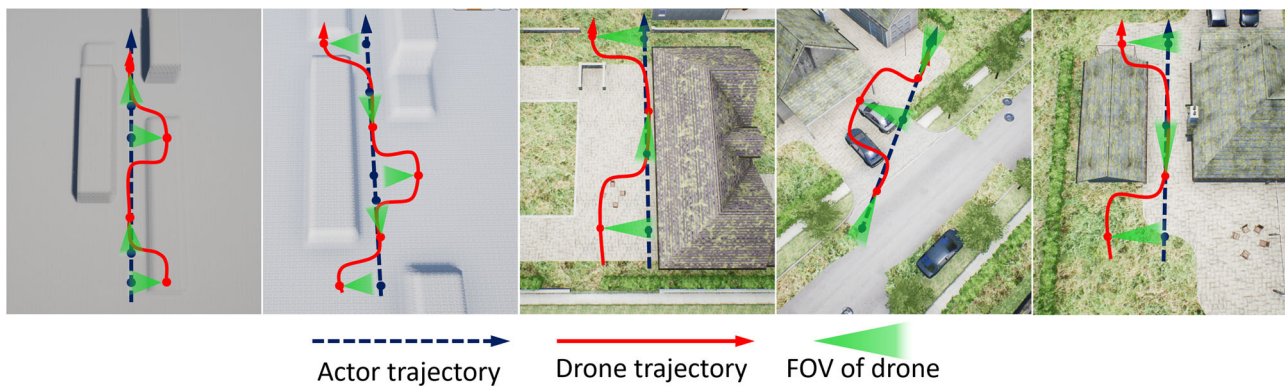


FIGURE 36 Drone trajectories of the highest-rated policies in the user study in Scenes 1–5 [Color figure can be viewed at [wileyonlinelibrary.com](#)]

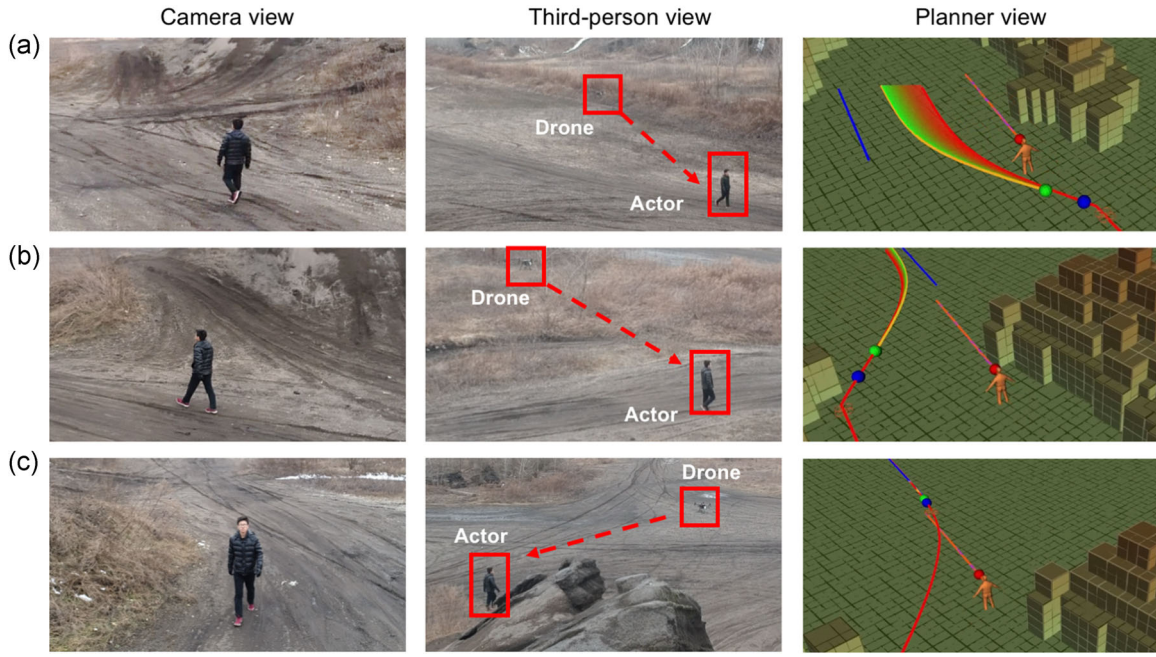


FIGURE 37 UAV follows an actor while switching shot types autonomously with our trained policy: (a) UAV starts at the back of the actor; (b) The mound's presence on the right-side of the actor leads to a left shot selection; (c) UAV switches to a frontal shot in the open area. UAV, unmanned aerial vehicle [Color figure can be viewed at wileyonlinelibrary.com]

10 | DISCUSSION

In this section, we discuss lessons learned throughout the development of our work, and also present comments on how our methods can be used with different types of sensors and UAV platforms.

10.1 | Lessons learned

During the development of our autonomous aerial cinematographer platform, we learned several lessons and gained insights into problem specificities, which we summarize below. We expect these lessons to not only be useful to researchers in the field of aerial vehicles, but also to generalize to other related areas.

Cascading errors can destabilize the robot

Estimation errors in a module get amplified if used downstream in decision-making. For example, we learned that jerky UAV movements lead to misregistration of camera pose, which leads to poor actor detection. This in turn leads to poor actor prediction, which can be off by meters. Unlike previous works that operate under highly precise motion capture systems, in real scenarios, we observe that controlling the camera orientation toward the position estimates causes the robot to completely lose the actor. To mitigate this effect, we chose to decouple motion planning, which uses the actor world projection estimates, from camera control, which uses only object detections on the current image as feedback. To validate the quality

of both threads independently, we performed statistical performance evaluations, as seen throughout Section 9.

Long-range sensors are beneficial to planning performance

The planner relies on the online map. Slow online map updates slow down the planner. This typically happens when the robot moves near large pockets of unknown areas, which triggers large updates for the TSDT. We learned that a relatively long-range LiDAR sensor maps out a significantly larger area. Hence almost always, the area near the robot is mapped out fully and the planner does not have to wait for map updates to enter an unknown region. While our system used a relatively large map of $250 \times 250 \times 100$ m, significantly faster mapping-planning frequencies could be achieved with the use of a smaller local map. Such change would likely be necessary with the use of shorter-range sensors like stereo pairs, which are common in commercial aircraft due to their reduced price.

Semisupervised methods can improve learning generalization

While deep learning methods are ubiquitous in computer vision, they rely on massive amounts of labeled data due to the complexity of the model class. Moreover, these models do not generalize to varying data distributions. We learned that one can reduce sample complexity by enforcing regularization/additional structure. In our case, we enforce temporal continuity on the network output. We show that a combination of *small labeled* data set for supervisory loss and a *large unlabeled* data set for temporal continuity loss is enough to solve the problem. Exploring other regularization techniques such

as consistency between different sensory modalities is also an interesting area to be investigated in the future.

Height estimate using IMU and barometer is not enough for long operations

During extended vehicle operations (over 5–10 min), we learned that the UAV's height calculated by fusing IMU and barometer data drifts significantly, especially after large vertical maneuvers. Inaccurate height estimates degrade pointcloud registration, thereby degrading the overall system performance. In the future, we plan to use LiDAR or visual SLAM to provide more accurate 3D localization.

Real-world noise reduces transferability of the artistic policy trained in simulation

The noise present in real-world testing conditions, in particular for the map registration and actor localization, affected the results generated by the policy that was trained purely in simulation using ground-truth data. Shot selection in simulation highly prioritized viewpoints that drew the UAV away from tall obstacles, while in deployment we observed that the drone avoided proximity to tall objects with a significantly smaller frequency. In the future we will consider artificially adding noise to simulations for better transferability, or training the artistic policy with a combination of simulated and real-life data.

10.2 | Adapting our work to different UAVs and sensors

In this study, we employed a long-range LiDAR sensor for mapping the environment and a DJI M210 UAV as the base platform. Even though we used relatively standard robotics development platforms and sensors, researchers and developers who work on problems similar to aerial cinematography may face different constraints in terms of payload capacity, vehicle size, sensor modalities, and costs. We argue that our problem formulation can be easily extended to other contexts.

First, we argue that the LiDAR sensor used in the online mapping module (Section 6) can be replaced by other sensors. Stereo cameras and depth sensors, for example, can be lightweight and significantly cheaper alternatives. The incoming hits for the mapping pipeline can then be acquired by using each pixel from a depth image, or each match from the stereo pair. The main advantage of LiDAR is the relatively long-range, in the order of hundreds of meters. When using lighter sensors, the developer needs to take into account the new sensor range to keep the UAV safe. They must consider the expected vehicle speed and the scale of obstacles in the environment so that the planner can reason about obstacles far from the UAV's current position.

In addition, our system architecture is platform-agnostic. Our methods can easily be adapted to smaller or potentially cheaper platforms. To do so, one only needs to care for the software interface between the trajectory controller and the aircraft's internal attitude or velocity controller.

In the future, we hope to see our architecture extended to other UAV types: our framework is not constrained to uniquely multirotors. With the appropriate changes in the motion planner's trajectory parametrization and cost functions, our pipeline can also be employed by fixed-wing or hybrid aircraft. More generally, despite the lower path dimensionality, even ground robots can employ the same methodology for visually tracking dynamic targets.

11 | CONCLUSION

In this study, we presented a complete system for robust autonomous aerial cinematography in unknown, unstructured environments while following dynamic actors in unscripted scenes. Current approaches do not address all theoretical and practical challenges present in real-life operation conditions; instead, they rely on simplifying assumptions such as requiring ground truth actor position, using prior maps of the environment, or only following one-shot type specified before the flight. To solve the entirety of the aerial cinematography, our system revolves around two key ideas. First, we frame the filming task as an efficient cost optimization problem, which allows trajectories with long time horizons to be computed in real-time, even under sensor noise. Second, instead of using hand-defined heuristics to guide the UAV's motion, we approach the artistic decision-making problem as a learning problem that can directly use human feedback.

We developed a system with four modules that work in parallel. (a) A vision-based actor localization module with motion prediction. (b) A real-time incremental mapping algorithm using a long-range LiDAR sensor. (c) A real-time optimization-based motion planner that exploits covariant gradients to efficiently calculate safe trajectories with long time horizons while balancing artistic objectives and occlusion avoidance for arbitrary obstacle shapes. (d) Finally, a deep RL policy for artistic viewpoint selection.

We offered extensive detailed experiments to evaluate the robustness and real-time performance of our system both in simulation and real-life scenarios. These experiments occur among a variety of terrain types, obstacle shapes, obstacle complexities, actor trajectories, actor types (i.e., people, cars, bikes) and shot types.

Based on our results, we identify several key directions for possible future work. One clear direction is the extension of our theory to multi-drone, multi-actor scenarios. This improvement can be achieved by the addition of new cost functions that penalize inter-drone collisions, inter-drone sight, and a metric for multi-actor coverage. In addition, multi-actor scenarios require slight modification in the definition of artistic parameters that define the desired artistic shot for our motion planner. Another interesting direction to follow lies in the reconstruction of dynamic scenes. While systems such as the CMU PanOptic Studio (Joo et al., 2015) can precisely reconstruct scenes volumetrically in indoor and static scenarios, to our knowledge, no current system offers a good volumetric reconstruction of dynamic scenes in natural environments in real-life conditions. Lastly, we envision further research in learning the artistic reasoning behind human choices. More broadly, as robotics evolves, autonomous agents are required to operate in a large variety of

tasks in proximity to humans, where success is in great part measured by the ability of the robot to execute esthetic and *human-like* behaviors. We identify important related areas to cinematography, such as autonomous driving and human–robot interaction, where fine nuances of human behavior modeling are important for the development of autonomous agents.

ACKNOWLEDGMENTS

We thank Xiangwei Wang and Greg Armstrong for the assistance in field experiments and robot construction. Research presented in this paper was funded by Yamaha Motor Co., Ltd. under award #A019969.

ORCID

- Rogerio Bonatti  <http://orcid.org/0000-0003-3015-9613>
 Wenshan Wang  <http://orcid.org/0000-0002-4488-5619>
 Cherie Ho  <http://orcid.org/0000-0003-1886-1020>
 Mirko Gschwindt  <http://orcid.org/0000-0002-7353-9141>
 Efe Camci  <http://orcid.org/0000-0002-5342-5163>
 Erdal Kayacan  <http://orcid.org/0000-0002-4873-2513>
 Sanjiban Choudhury  <http://orcid.org/0000-0003-2762-8888>
 Sebastian Scherer  <http://orcid.org/0000-0002-8373-4688>

REFERENCES

- Aine, S., Swaminathan, S., Narayanan, V., Hwang, V., & Likhachev, M. (2016). Multi-heuristic A. *The International Journal of Robotics Research*, 35(1-3), 224–243.
- Arijon, D. (1976). Grammar of the film language.
- Bonatti, R., Ho, C., Wang, W., Choudhury, S., & Scherer, S. (2019). Towards a robust aerial cinematography platform: Localizing and tracking moving targets in unstructured environments. *2019 IEEE/RSJ International Conference on Intelligent Robots and Systems (IROS)*.
- Bonatti, R., Zhang, Y., Choudhury, S., Wang, W., & Scherer, S. (2018). Autonomous drone cinematographer: Using artistic principles to create smooth, safe, occlusion-free trajectories for aerial filming. *International Symposium on Experimental Robotics*.
- Bowen, C. J., & Thompson, R. (2013). *Grammar of the shot*. Abingdon, OX: Taylor & Francis.
- Boyd, S., & Vandenberghe, L. (2004). *Convex optimization*. New York, NY: Cambridge University Press.
- Cao, Z., Simon, T., Wei, S., & Sheikh, Y. (2017). Realtime multi-person 2D pose estimation using part affinity fields. *2017 IEEE Conference on Computer Vision and Pattern Recognition (CVPR)*, IEEE (pp. 1302–1310).
- Charrow, B., Kahn, G., Patil, S., Liu, S., Goldberg, K., Abbeel, P., & Kumar, V. (2015). Information-theoretic planning with trajectory optimization for dense 3d mapping. *Robotics: Science and Systems* (Vol. 11), Rome.
- Choi, J., Lee, B.-J., & Zhang, B.-T. (2016). Human body orientation estimation using convolutional neural network. arXiv preprint, arXiv:1609.01984.
- Choudhury, S., Gammell, J. D., Barfoot, T. D., Srinivasa, S. S., & Scherer, S. (2016). Regionally accelerated batch informed trees (rabbit): A framework to integrate local information into optimal path planning. *2016 IEEE International Conference on Robotics and Automation (ICRA)*, IEEE (pp. 4207–4214).
- Christiano, P. F., Leike, J., Brown, T., Martic, M., Legg, S., & Amodei, D. (2017). Deep reinforcement learning from human preferences. *Advances in Neural Information Processing Systems*, 4299–4307.
- Christie, M., Olivier, P., & Normand, J.-M. (2008). Camera control in computer graphics. *Computer Graphics Forum*, 27, 2197–2218.
- Cover, H., Choudhury, S., Scherer, S., & Singh, S. (2013). Sparse tangential network (spartan): Motion planning for micro aerial vehicles. *2013 IEEE International Conference on Robotics and Automation*, IEEE (pp. 2820–2825).
- Dai, Z., Yang, Z., Yang, F., Cohen, W. W., & Salakhutdinov, R. R. (2017). Good semi-supervised learning that requires a bad gan. *Advances in Neural Information Processing Systems* (pp. 6513–6523).
- De-Miguel-Molina, M. (2018). *Ethics and civil drones: European policies and proposals for the industry*. Cham: Springer.
- Deng, Z., Si, W., Qu, Z., Liu, X., & Na, Z. (2017). Heading estimation fusing inertial sensors and landmarks for indoor navigation using a smartphone in the pocket. *EURASIP Journal on Wireless Communications and Networking*, 2017(1), 160.
- DJI. (2018). DJI mavic. Retrieved from <https://www.dji.com/mavic>
- Drucker, S. M., & Zeltzer, D. (1994). Intelligent camera control in a virtual environment. *Proceedings of Graphics Interface* (pp. 190–190).
- Elbanhawi, M., & Simic, M. (2014). Sampling-based robot motion planning: A review. *IEEE Access*, 2, 56–77.
- Fang, H., & Zhang, M. (2017). Creatism: A deep-learning photographer capable of creating professional work. arXiv preprint, arXiv:1707.03491
- Flohr, F., Dumitru-Guzu, M., Kooij, J. F., & Gavrila, D. M. (2015). A probabilistic framework for joint pedestrian head and body orientation estimation. *IEEE Transactions on Intelligent Transportation Systems*, 16(4), 1872–1882.
- Galvane, Q., Fleureau, J., Tariolle, F.-L., & Guillotel, P. (2017). Automated cinematography with unmanned aerial vehicles. arXiv preprint, arXiv: 1712.04353
- Galvane, Q., Lino, C., Christie, M., Fleureau, J., Servant, F., Tariolle, F., & Guillotel, P. (2018). Directing cinematographic drones. *ACM Transactions on Graphics (TOG)*, 37(3), 34.
- Gatys, L. A., Ecker, A. S., & Bethge, M. (2016). Image style transfer using convolutional neural networks. *Proceedings of the IEEE Conference on Computer Vision and Pattern Recognition* (pp. 2414–2423).
- Gebhardt, C., Hepp, B., Nägeli, T., Stević, S., & Hilliges, O. (2016). Airways: Optimization-based planning of quadrotor trajectories according to high-level user goals. *Proceedings of the 2016 CHI Conference on Human Factors in Computing Systems*, ACM (pp. 2508–2519).
- Gebhardt, C., Stević, S., & Hilliges, O. (2018). Optimizing for aesthetically pleasing qdrorot camera motion. *ACM Transactions on Graphics (TOG)*, 37(4), 90.
- Geiger, A., Lenz, P., Stiller, C., & Urtasun, R. (2013). Vision meets robotics: The kitti dataset. *International Journal of Robotics Research (IJRR)*, 32, 1231–1237.
- Gleicher, M., & Witkin, A. (1992). Through-the-lens camera control. *ACM SIGGRAPH Computer Graphics*, 26, 331–340.
- Goroshin, R., Bruna, J., Tompson, J., Eigen, D., & LeCun, Y. (2015). Unsupervised learning of spatiotemporally coherent metrics. *Proceedings of the IEEE International Conference on Computer Vision* (pp. 4086–4093).
- Gschwindt, M., Camci, E., Bonatti, R., Wang, W., Kayacan, E., & Scherer, S. (2019). Can a robot become a movie director? Learning artistic principles for aerial cinematography. *2019 IEEE/RSJ International Conference on Intelligent Robots and Systems (IROS)*.
- Henriques, J. F., Caseiro, R., Martins, P., & Batista, J. (2015). High-speed tracking with kernelized correlation filters. *IEEE Transactions on Pattern Analysis and Machine Intelligence*, 37(3), 583–596.
- Hoffer, E., & Ailon, N. (2016). Semi-supervised deep learning by metric embedding. arXiv preprint, arXiv:1611.01449
- Howard, A. G., Zhu, M., Chen, B., Kalenichenko, D., Wang, W., Weyand, T., & Adam, H. (2017). Mobilenets: Efficient convolutional neural networks for mobile vision applications. arXiv preprint, arXiv:1704.04861
- Huang, C., Gao, F., Pan, J., Yang, Z., Qiu, W., Chen, P., & Cheng, K.-T. T. (2018). Act: An autonomous drone cinematography system for action

- scenes. 2018 IEEE International Conference on Robotics and Automation (ICRA), IEEE (pp. 7039–7046).
- Huang, C., Yang, Z., Kong, Y., Chen, P., Yang, X., & Cheng, K.-T. T. (2018). Through-the-lens drone filming. 2018 IEEE/RSJ International Conference on Intelligent Robots and Systems (IROS), IEEE (pp. 4692–4699).
- Huber, P. J. (1964). Robust estimation of a location parameter. *The Annals of Mathematical Statistics*, 35(1), 73–101.
- Ionescu, C., Papava, D., Olaru, V., & Sminchisescu, C. (2014). Human3.6 m: Large scale datasets and predictive methods for 3d human sensing in natural environments. *IEEE Transactions on Pattern Analysis and Machine Intelligence*, 36(7), 1325–1339.
- Isler, S., Sabzevari, R., Delmerico, J., & Scaramuzza, D. (2016). An information gain formulation for active volumetric 3d reconstruction. 2016 IEEE International Conference on Robotics and Automation (ICRA), IEEE (pp. 3477–3484).
- Joo, H., Liu, H., Tan, L., Gui, L., Nabbe, B., Matthews, I., & Sheikh, Y. (2015). Panoptic studio: A massively multiview system for social motion capture. *Proceedings of the IEEE International Conference on Computer Vision* (pp. 3334–3342).
- Joubert, N., Goldman, D. B., Berthouzoz, F., Roberts, M., Landay, J. A., & Hanrahan, P. (2016). Towards a drone cinematographer: Guiding quadrotor cameras using visual composition principles. arXiv preprint, arXiv:1610.01691
- Joubert, N., Roberts, M., Truong, A., Berthouzoz, F., & Hanrahan, P. (2015). An interactive tool for designing quadrotor camera shots. *ACM Transactions on Graphics (TOG)*, 34(6), 238.
- Karaman, S., & Frazzoli, E. (2011). Sampling-based algorithms for optimal motion planning. *The International Journal of Robotics Research*, 30(7), 846–894.
- Karpathy, A. (2015). What a deep neural network thinks about your #selfie, Andrej Karpathy Blog. karpathy.github.io.
- Kingma, D. P., & Ba, J. (2014). Adam: A method for stochastic optimization. arXiv preprint, arXiv:1412.6980
- Kitani, K. M., Ziebart, B. D., Bagnell, J. A., & Hebert, M. (2012). Activity forecasting. In A. Fitzgibbon, S. Lazebnik, P. Perona, Y. Sato & C. Schmid (Eds.), *European Conference on Computer Vision 2012* (Vol. 7575, pp. 201–214). Berlin: Springer.
- Klingensmith, M., Dryanovski, I., Srinivasa, S., & Xiao, J. (2015). Chisel: Real time large scale 3d reconstruction onboard a mobile device using spatially hashed signed distance fields. *Robotics: Science and Systems* (Vol. 4).
- Krishnamurthy, A., Agarwal, A., & Langford, J. (2016). Contextual-mdps for pacreinforcement learning with rich observations. arXiv preprint, arXiv:1602.02722.
- Kuffner, J., & LaValle, S. (2000). Rrt-connect: An efficient approach to single-query path planning. Proceedings 2000 ICRA. Millennium Conference. IEEE International Conference on Robotics and Automation. Symposia Proceedings (Cat. No. 00CH37065), IEEE (Vol. 2, pp. 995–1001).
- LaBella, L. (2016). *Drones and entertainment*. New York, NY: The Rosen Publishing Group, Inc.
- Lan, Z., Shridhar, M., Hsu, D., & Zhao, S. (2017). Xpose: Reinventing user interaction with flying cameras. *Proceedings of Robotics: Science and Systems*.
- LaValle, S. M. (2006). *Planning algorithms*. Cambridge: Cambridge University Press. <http://planning.cs.uiuc.edu/>
- Leake, M., Davis, A., Truong, A., & Agrawala, M. (2017). Computational video editing for dialogue-driven scenes. *ACM Trans. Graph.* 36(4), 130–131.
- Lin, T.-Y., Maire, M., Belongie, S., Hays, J., Perona, P., Ramanan, D., Dollár, P., & Zitnick, C. L. (2014). Microsoft coco: Common objects in context. *European conference on computer vision*, Springer (pp. 740–755).
- Lino, C., & Christie, M. (2015). Intuitive and efficient camera control with the toric space. *ACM Transactions on Graphics (TOG)*, 34(4), 82.
- Lino, C., Christie, M., Ranon, R., & Bares, W. (2011). The director's lens: an intelligent assistant for virtual cinematography. *Proceedings of the 19th ACM international conference on Multimedia*, ACM (pp. 323–332).
- Liu, D., Pei, L., Qian, J., Wang, L., Liu, P., Dong, Z., & Wei, W. (2016). A novel heading estimation algorithm for pedestrian using a smartphone without attitude constraints. *Ubiquitous Positioning, Indoor Navigation and Location Based Services (UPINLBS). 2016 Fourth International Conference on ubiquitous Positioning, Indoor Navigation and Location Based Services (UPINLBS)*, IEEE (pp. 29–37).
- Liu, P., Liu, W., & Ma, H. (2017). Weighted sequence loss based spatial-temporal deep learning framework for human body orientation estimation. *Multimedia and Expo (ICME). 2017 IEEE International Conference on Multimedia and Expo (ICME)*, IEEE (pp. 97–102).
- Liu, W., Anguelov, D., Erhan, D., Szegedy, C., Reed, S., Fu, C.-Y., & Berg, A. C. (2016). SSD: Single shot multibox detector. *European conference on computer vision*, Springer (pp. 21–37).
- Liu, W., Zhang, Y., Tang, S., Tang, J., Hong, R., & Li, J. (2013). Accurate estimation of human body orientation from rgb-d sensors. *IEEE Transactions on Cybernetics*, 43(5), 1442–1452.
- Luna, R., Şucan, I. A., Moll, M., & Kavraki, L. E. (2013). Anytime solution optimization for sampling-based motion planning. 2013 IEEE International Conference on Robotics and Automation, IEEE (pp. 5068–5074).
- Mnih, V., Kavukcuoglu, K., Silver, D., Graves, A., Antonoglou, I., Wierstra, D., & Riedmiller, M. (2013). Playing atari with deep reinforcement learning. arXiv preprint, arXiv:1312.5602
- Mnih, V., Kavukcuoglu, K., Silver, D., Rusu, A. A., Veness, J., Bellemare, M. G., & Ostrovski, G. (2015). Human-level control through deep reinforcement learning. *Nature*, 518(7540), 529.
- Mobahi, H., Collobert, R., & Weston, J. (2009). Deep learning from temporal coherence in video. *Proceedings of the 26th Annual International Conference on Machine Learning*, ACM (pp. 737–744).
- Nägeli, T., Meier, L., Domahidi, A., Alonso-Mora, J., & Hilliges, O. (2017). Real-time planning for automated multi-view drone cinematography. *ACM Transactions on Graphics (TOG)*, 36(4), 132.
- Nene, S. A., Nayar, S. K., & Murase, H. (1996). Columbia object image library (coil-20).
- Newcombe, R. A., Izadi, S., Hilliges, O., Molynaux, D., Kim, D., Davison, A. J., & Fitzgibbon, A. (2011). Kinectfusion: Real-time dense surface mapping and tracking. 2011 10th IEEE International Symposium on Mixed and Augmented Reality (ISMAR), IEEE (pp. 127–136).
- Oh, S., Hoogs, A., Perera, A., Cuntoor, N., Chen, C.-C., Lee, J. T., & Davis, L. (2011). A large-scale benchmark dataset for event recognition in surveillance video. 2011 IEEE Conference on Computer Vision and Pattern Recognition (CVPR), IEEE (pp. 3153–3160).
- Oleynikova, H., Taylor, Z., Fehr, M., Nieto, J., & Siegwart, R. (2016). Voxblox: Building 3d signed distance fields for planning. arXiv, arXiv-1611.
- Penin, B., Giordano, P. R., & Chaumette, F. (2018). Vision-based reactive planning for aggressive target tracking while avoiding collisions and occlusions. *IEEE Robotics and Automation Letters*, 3(4), 3725–3732.
- Quigley, M., Conley, K., Gerkey, B., Faust, J., Foote, T., Leibs, J., & Ng, A. Y. (2009). Ros: an open-source robot operating system. *ICRA Workshop on Open Source Software*, Kobe, Japan (Vol. 3, p. 5).
- Raman, R., Sa, P. K., Majhi, B., & Bakshi, S. (2016). Direction estimation for pedestrian monitoring system in smart cities: An hmm based approach. *IEEE Access*, 4, 5788–5808.
- Rasmus, A., Berglund, M., Honkala, M., Valpola, H., & Raiko, T. (2015). Semi-supervised learning with ladder networks. *Advances in Neural Information Processing Systems* (pp. 3546–3554).
- Ratliff, N., Zucker, M., Bagnell, J. A., & Srinivasa, S. (2009). CHOMP: Gradient optimization techniques for efficient motion planning. *IEEE International Conference on Robotics and Automation, 2009. ICRA'09*, IEEE (pp. 489–494).
- Ratliff, N. D., Silver, D., & Bagnell, J. A. (2009). Learning to search: Functional gradient techniques for imitation learning. *Autonomous Robots*, 27(1), 25–53.

- Redmon, J., Divvala, S., Girshick, R., & Farhadi, A. (2016). You only look once: Unified, real-time object detection. *Proceedings of the IEEE Conference on Computer Vision and Pattern Recognition* (pp. 779–788).
- Ren, S., He, K., Girshick, R., & Sun, J. (2015). Faster R-CNN: Towards real-time object detection with region proposal networks. *Advances in Neural Information Processing Systems* (pp. 91–99).
- Ristani, E., Solera, F., Zou, R., Cucchiara, R., & Tomasi, C. (2016). Performance measures and a data set for multi-target, multi-camera tracking. *European Conference on Computer Vision Workshop on Benchmarking Multi-Target Tracking*.
- Roberts, M., & Hanrahan, P. (2016). Generating dynamically feasible trajectories for quadrotor cameras. *ACM Transactions on Graphics (TOG)*, 35(4), 61.
- Santamarina-Campos, V., & Segarra-Oña, M. (2018). Introduction to drones and technology applied to the creative industry. AIRT project: An overview of the main results and actions, *Drones and the Creative Industry* (pp. 1–17). Cham: Springer.
- Schulman, J., Ho, J., Lee, A., Awwal, I., Bradlow, H., & Abbeel, P. (2013). Finding locally optimal, collision-free trajectories with sequential convex optimization. *Robotics: Science and Systems*, 9, 1–10.
- Shah, S., Dey, D., Lovett, C., & Kapoor, A. (2018). Airsim: High-fidelity visual and physical simulation for autonomous vehicles, *Field and service robotics* (pp. 621–635). London: Springer.
- Skydio. (2018). Skydio r1 self-flying camera. Retrieved from <https://www.skydio.com/technology/>
- Soomro, K., Zamir, A. R., & Shah, M. (2012). Ucf101: A dataset of 101 human actions classes from videos in the wild. arXiv preprint, arXiv:1212.0402.
- Srivastava, N., Mansimov, E., & Salakhudinov, R. (2015). Unsupervised learning of video representations using LSTMS. *International Conference On Machine Learning* (pp. 843–852).
- Stavens, D., & Thrun, S. (2010). Unsupervised learning of invariant features using video. *2010 IEEE Conference on Computer Vision and Pattern Recognition (CVPR)*, IEEE (pp. 1649–1656).
- Strigel, E., Meissner, D., Seeliger, F., Wilking, B., & Dietmayer, K. (2014). The ko-per intersection laserscanner and video dataset. *17th International IEEE Conference on Intelligent Transportation Systems (ITSC)*, IEEE (pp. 1900–1901).
- Sutton, R. S., & Barto, A. G. (1998). *Reinforcement learning: An introduction* (Vol. 1). Cambridge: MIT Press.
- Thrun, S., Burgard, W., & Fox, D. (2005). *Probabilistic robotics*. Cambridge: MIT Press.
- Tian, R., Li, L., Yang, K., Chien, S., Chen, Y., & Sherony, R. (2014). Estimation of the vehicle-pedestrian encounter/conflict risk on the road based on tasi 110-car naturalistic driving data collection. *2014 IEEE Intelligent Vehicles Symposium Proceedings*, IEEE (pp. 623–629).
- Toshev, A., & Szegedy, C. (2014). Deeppose: Human pose estimation via deep neural networks. *Proceedings of the IEEE Conference on Computer Vision and Pattern Recognition* (pp. 1653–1660).
- Urmson, C., Anhalt, J., Bagnell, D., Baker, C., Bittner, R., Clark, M., & Ziglar, J. (2008). Autonomous driving in urban environments: Boss and the urban challenge. *Journal of Field Robotics*, 25(8), 425–466.
- Vázquez, M., Steinfeld, A., & Hudson, S. E. (2015). Parallel detection of conversational groups of free-standing people and tracking of their lower-body orientation. *2015 IEEE/RSJ International Conference on Intelligent Robots and Systems (IROS)*, IEEE (pp. 3010–3017).
- Vista, F. P., Lee, D.-J., & Chong, K. T. (2015). Design of an EKF-CI based sensor fusion for robust heading estimation of marine vehicle. *International Journal of Precision Engineering and Manufacturing*, 16(2), 403–407.
- Wang, C., Fang, Y., Zhao, H., Guo, C., Mita, S., & Zha, H. (2016). Probabilistic inference for occluded and multiview on-road vehicle detection. *IEEE Transactions on Intelligent Transportation Systems*, 17(1), 215–229.
- Wang, W., Ahuja, A., Zhang, Y., Bonatti, R., & Scherer, S. (2019). Improved generalization of heading direction estimation for aerial filming using semi-supervised regression. *2019 IEEE International Conference on Robotics and Automation (ICRA)*.
- Wang, X., & Gupta, A. (2015). Unsupervised learning of visual representations using videos. *Proceedings of the 2015 IEEE International Conference on Computer Vision (ICCV)*, IEEE Computer Society (pp. 2794–2802).
- Weston, J., Ratle, F., Mobahi, H., & Collobert, R. (2012). Deep learning via semi-supervised embedding, *Neural Networks: Tricks of the Trade* (pp. 639–655). Berlin, Heidelberg: Springer.
- Wu, H.-Y., Palù, F., Ranon, R., & Christie, M. (2018). Thinking like a director: Film editing patterns for virtual cinematographic storytelling. *ACM Transactions on Multimedia Computing, Communications, and Applications (TOMM)*, 14(4), 81.
- Xie, K., Yang, H., Huang, S., Lischinski, D., Christie, M., Xu, K., & Huang, H. (2018). Creating and chaining camera moves for quadrotor videography. *ACM Transactions on Graphics*, 37, 14.
- Zhang, Y., Wang, W., Bonatti, R., Maturana, D., & Scherer, S. (2018). Integrating kinematics and environment context into deep inverse reinforcement learning for predicting off-road vehicle trajectories. *Conference on Robot Learning* (pp. 894–905).
- Zou, W., Zhu, S., Yu, K., & Ng, A. Y. (2012). Deep learning of invariant features via simulated fixations in video. *Advances in Neural Information Processing Systems* (pp. 3203–3211).
- Zucker, M., Ratliff, N., Dragan, A. D., Pivtoraiko, M., Klingensmith, M., Dellin, C. M., & Srinivas, S. S. (2013). CHOMP: Covariant hamiltonian optimization for motion planning. *The International Journal of Robotics Research*, 32(9–10), 1164–1193.

SUPPORTING INFORMATION

Additional supporting information may be found online in the Supporting Information section.

How to cite this article: Bonatti R, Wang W, Ho C, et al. Autonomous aerial cinematography in unstructured environments with learned artistic decision-making. *J Field Robotics*. 2020;1–36.
<https://doi.org/10.1002/rob.21931>

APPENDIX A: DERIVATIONS OF PLANNING COST FUNCTIONS

A.1 Smoothness cost

We can discretize Equation (8) to compute the smoothness for ξ_q :

$$J_{\text{smooth}}(\xi_q) = \frac{1}{(n-1)} \frac{1}{2} \sum_{t=1}^{n-1} \left[\alpha_0 \left| \frac{p_t - p_{t-1}}{\Delta t} \right|^2 + \alpha_1 \left| \frac{\dot{p}_t - \dot{p}_{t-1}}{\Delta t} \right|^2 + \alpha_2 \left| \frac{\ddot{p}_t - \ddot{p}_{t-1}}{\Delta t} \right|^2 + \dots \right]. \quad (\text{A1})$$

To simplify Equation (A1), we define: $\Delta t = \frac{t_f}{n-1}$, a finite differentiation operator K , and an auxiliary matrix e for the contour conditions:

$$K_{(n-1) \times (n-1)} = \begin{bmatrix} 1 & 0 & 0 & \cdots & 0 & 0 & 0 \\ -1 & 1 & 0 & \cdots & 0 & 0 & 0 \\ 0 & -1 & 1 & \cdots & 0 & 0 & 0 \\ \vdots & & & & & & \\ 0 & 0 & 0 & 0 & \cdots & 0 & -1 & 1 \end{bmatrix}$$

$$e_{(n-1) \times 3} = \begin{bmatrix} -p_{0x} & -p_{0y} & -p_{0z} \\ 0 & 0 & 0 \\ \vdots & \vdots & \vdots \\ 0 & 0 & 0 \end{bmatrix}. \quad (\text{A2})$$

By manipulating the terms K , e , and Δt we obtain the auxiliary terms:

$$\begin{aligned} K_0 &= \frac{K}{\Delta t}, \quad e_0 = \frac{e}{\Delta t}, \\ K_1 &= \frac{K^2}{\Delta t^2}, \quad e_1 = \frac{Ke}{\Delta t^2} + \frac{\dot{e}}{\Delta t^2}, \\ K_2 &= \frac{K^3}{\Delta t^3}, \quad e_2 = \frac{K^2e}{\Delta t^3} + \frac{K\dot{e}}{\Delta t^3} + \frac{\ddot{e}}{\Delta t^3}. \end{aligned} \quad (\text{A3})$$

$$\begin{aligned} A_0 &= K_0^T K_0, \quad b_0 = K_0^T e_0, \quad c_0 = e_0^T e_0, \\ A_1 &= K_1^T K_1, \quad b_1 = K_1^T e_1, \quad c_1 = e_1^T e_1, \\ A_2 &= K_2^T K_1, \quad b_2 = K_2^T e_2, \quad c_2 = e_2^T e_2. \end{aligned} \quad (\text{A4})$$

Finally, we can analytically write the smoothness cost as a quadratic objective:

$$J_{\text{smooth}}(\xi_q) = \frac{1}{2(n-1)} \text{Tr}(\xi_q^T A_{\text{smooth}} \xi_q + 2\xi_q^T b_{\text{smooth}} + c_{\text{smooth}}) \quad (\text{A5})$$

where: $A_{\text{smooth}} = \alpha_0 A_0 + \alpha_1 A_1 + \dots$
 $b_{\text{smooth}} = \alpha_0 b_0 + \alpha_1 b_1 + \dots$
 $c_{\text{smooth}} = \alpha_0 c_0 + \alpha_1 c_1 + \dots$

Since $J_{\text{smooth}}(\xi_q)$ is quadratic, we find analytic expressions for its gradient and Hessian. Note that the Hessian expression does not depend on the current trajectory, which is a property used to speed up the optimization algorithm described in Section 7.4:

$$\begin{aligned} \nabla J_{\text{smooth}}(\xi_q) &= \frac{1}{(n-1)} (A_{\text{smooth}} \xi_q + b_{\text{smooth}}), \\ \nabla^2 J_{\text{smooth}}(\xi_q) &= \frac{1}{(n-1)} A_{\text{smooth}}. \end{aligned} \quad (\text{A6})$$

A.2 Shot quality cost

We can calculate J_{shot} in the discrete form

$$J_{\text{shot}}(\xi_q, \xi_a) = \frac{1}{(n-1)} \frac{1}{2} \sum_{t=1}^n |p_t - p_t^{\text{shot}}|^2. \quad (\text{A7})$$

By defining auxiliary matrices, we can also define a quadratic expression

$$J_{\text{shot}}(\xi_q, \xi_a) = \frac{1}{2(n-1)} \text{Tr}(\xi_q^T A_{\text{shot}} \xi_q + 2\xi_q^T b_{\text{shot}} + c_{\text{shot}}), \quad (\text{A8})$$

where

$$K_{\text{shot}} = -I_{(n-1) \times (n-1)}$$

$$e_{\text{shot}} = \xi_{\text{shot}} = \begin{bmatrix} p_{1x}^{\text{shot}} & p_{1y}^{\text{shot}} & p_{1z}^{\text{shot}} \\ p_{1x}^{\text{shot}} & p_{1y}^{\text{shot}} & p_{1z}^{\text{shot}} \\ \vdots & \vdots & \vdots \\ p_{(n-1)x}^{\text{shot}} & p_{(n-1)y}^{\text{shot}} & p_{(n-1)z}^{\text{shot}} \end{bmatrix}, \quad (\text{A9})$$

and

$$A_{\text{shot}} = K_{\text{shot}}^T K_{\text{shot}}, \quad b_{\text{shot}} = K_{\text{shot}}^T e_{\text{shot}}, \quad c_{\text{shot}} = e_{\text{shot}}^T e_{\text{shot}}. \quad (\text{A10})$$

We can again find analytic expressions for the shot quality gradient and Hessian, which is independent from the current trajectory

$$\begin{aligned} \nabla J_{\text{shot}}(\xi_q) &= \frac{1}{(n-1)} (A_{\text{shot}} \xi_q + b_{\text{shot}}), \\ \nabla^2 J_{\text{shot}}(\xi_q) &= \frac{1}{(n-1)} A_{\text{shot}}. \end{aligned} \quad (\text{A11})$$